

Computational and Experimental Analysis of Early Reflections in Concert Spaces

Wen Xiao



Music Technology Area, Department of Music Research
Schulich School of Music
McGill University
Montreal, Canada

October 2017

A thesis submitted to McGill University in partial fulfillment of the requirements for the degree of Master of Arts in Music Technology.

© 2017 Wen Xiao

Abstract

A study on the acoustic simulations of early reflections in three-dimensional rooms is presented. Measurements of four real rooms in Schulich School of Music and computational simulations in Matlab are compared to verify the results.

The four real rooms are modeled with two methods commonly used in modern geometric acoustic modeling, the image source method and the ray-tracing method. Then the simulation results are compared with the measurement in impulse responses and echo densities [1]. Discussions about the differences between measurements and modeling results are based on geometrical models and acoustic properties. Factors influencing the accuracy of the simulations include the geometric shapes of rooms, the directivity patterns of the speakers and microphones in the measurement and acoustic coefficients such as wall absorption coefficients and air absorption coefficients. The results indicate that rooms commonly used for music performance have very diffuse scattering characteristics, which has important implications for modeling techniques based on assumptions of specular reflections. As well, this may have some consequences on our understanding of sound localization, which assumes specular early reflections. Suggestions for further improvements of models and measurement techniques are given.

Sommaire

Une étude sur les simulations acoustiques des réflexions précoces dans les salles tridimensionnelles est présentée. Les mesures de quatre salles dans l'École de musique Schulich et les simulations calculées par Matlab sont comparées pour vérifier les résultats.

Les quatre salles existantes sont modelées avec deux méthodes couramment utilisées dans la modélisation acoustique géométrique moderne, la méthode source d'image et la méthode de lançage de rayons. Les résultats des mesures de réponses impulsionnelles et des densités d'échos de la simulation sont comparés [1]. Les discussions sur les différences entre les mesures et les résultats de la modélisation sont basées sur des modèles géométriques et des propriétés acoustiques. Les facteurs influençant la précision des simulations incluent les formes géométriques des salles, les modèles de directivité des haut-parleurs et des microphones mesurés et les coefficients acoustiques tels que les coefficients d'absorption des parois et de l'air. Les résultats indiquent que les salles couramment utilisées pour les performances musicaux ont des caractéristiques de diffusion d'ondes très diffuses, ce qui a des implications importantes pour les techniques de modélisation basées sur des hypothèses de réflexions spéculaires. Cela peut avoir des conséquences sur notre compréhension de la localisation du son, qui suppose une spécification de réflexions préliminaires. Des suggestions pour d'autres améliorations des modèles et des techniques de mesure sont données.

Acknowledgments

I gratefully thank my supervisor Dr. Gary Scavone for encouraging me to choose a topic in which I can develop my own interest. I would like to show my great appreciation to Gary for helping me ensure my essential measurements worked smoothly and spending considerable time on advising and revising my thesis with patient guidance and support. I would extend my appreciation to Romain Dumoulin for helping me proof my algorithms and sharing insight into my topic.

Many thanks to the members of the Computational Acoustics Modeling Laboratory (CAML): Connor, Esteban, Lei, Negin, Quim and Song, as well as my colleagues at the Music Technology Area: Alex, Ian, Johny, Julien, Lingxiao, Martha, Olafur, Yaolong and Yong for their advice and friendship. Thank you Darryl Cameron for your technical assistance. Thank you Yves Mthot, Julien Boissinot and other members in CIRMMT for lending me instruments for measurements. Thanks to Professor George Massenburg and the other colleagues in sound recording area for providing recording method and related data. Specially thanks to Suyu Ding for kindly providing proof reading.

I would also like to thank my friends who have experienced the precious time with me. At last, I give my greatest appreciation to my parents for their gift of courage and wisdom to help me overcome obstacles and difficulties throughout my study.

Contents

1	Introduction	1
1.1	Motivation	1
1.2	Outline	2
1.3	Contributions	3
2	Geometric Acoustic Techniques	4
2.1	Basic Geometric Acoustics	4
2.1.1	Wave Propagation	4
2.1.2	Sound Absorption	7
2.1.3	Sound Diffusion	9
2.1.4	The Impulse Response	9
2.1.5	Acoustic levels	11
2.2	The Image Source Method (ISM)	12
2.3	The Ray-Tracing Method	15
2.4	Related Applications	18
2.4.1	Odeon	18
2.4.2	Catt-Acoustic	18
3	Model Implementation in 3D Enclosures	21
3.1	Image Source Method Modeling	21
3.1.1	Digital Constructions of Rooms	21
3.1.2	Source Imaging Process	23
3.1.3	Path Validity Detection	24
3.1.4	Energy Calculation	29
3.2	Ray-tracing Approach	30

3.2.1	Ray Direction Initialization	30
3.2.2	Initial Ray Number Determination	32
3.2.3	Sound Ray Reception	33
3.3	Echo Density	35
4	Measurements and Modeling Results	37
4.1	Room Measuring Methods	38
4.2	Room Details and Results	40
4.2.1	The Music Multimedia Room (MMR)	41
4.2.2	Pollack Hall	49
4.2.3	Tanna Schulich Hall	53
4.2.4	The Wirth Opera Studio	56
4.3	Summary of Results	59
5	Conclusions and Future Work	60
A	Details of Measured Rooms	62

List of Figures

2.1	Sound propagation through the air (based on [2]).	5
2.3	General reflection process.	8
2.4	Impulse response of a room representing the propagation of sound pressure from a source to a receiver (based on [3]).	10
2.5	(a) Graph interpreting the Image Source Method (from [4]). (b) Building the second order ray path (from [4]).	12
2.6	(a) The distribution of image sources in a rectangular room (from [5]). (b) An example of an overlaped image source building.	13
2.7	The principle of the ray tracing technique (based on [6]).	15
2.8	The flow diagram of the ray tracing algorithm (based on [7]).	16
2.9	Odeon acoustics simulation software.	19
2.10	Catt-Acoustics acoustics simulation software.	20
3.1	A plane obtained from three points (based on [3]).	22
3.2	An image source obtained with Gram-Schmidt algorithm.	24
3.3	In-path test on the image source. S denotes to the original sound source, S' is one image source of S , R represents the receiver, the intruding wall is the reflecting surface, and P is the intersection point. The path in b is invalid due to the position of the intersection point lying out of the path.	25
3.4	The in-polygon test in ISM algorithm.	26
3.5	An example of a path obstructed by a wall in a room. The path is invalid because the segment $\overline{RP_1}$ is truncated by the extruded wall.	27

3.6	Building the ray path with the Image Source Method (based on [8]). (a) Path $S-P_1-P_2-R$ is obtained by mirroring the source to the two surfaces marked in the picture. (b) The first collision point P_1 can be obtained by simultaneously mirroring the receiver and the second-order image source on the first mirror.	28
3.7	Sound source is divided into uniform areas to generate ray directions. . . .	31
3.8	Energy response of a impulse response implemented by the Ray-Tracing Method. The time of every interval is 0.01s, containing 480 samples in the sample rate of 48KHz.	33
3.9	Magnitude of fluctuations of four rooms measure in the experiments. Each curve takes an average of 20 runs.	34
3.10	Measured room impulse response (blue, 48 kHz samples) and its echo density profiles in different window sizes: 0.01(red), 0.02(yellow) and 0.03(purple)s. Note that the time axis is logarithmic.	36
4.1	Approximated directivity of the speaker in the model.	38
4.2	Views of Music Multimedia Room and its 3D model. The blue point represents the position of the speaker S_1 , the red point represents the first position of the microphone R_1 , the yellow point represents the second position of the microphone R_2 , the purple point denotes the third position of the microphone R_3 . All the points' coordinates are listed in Table 4.4. . . .	41
4.3	Comparison between measured impulse responses and modelled impulse responses with the Image Source Method in different octave bands. The source and the receivers' positions are at S_1 and R_1	44
4.4	Impulse responses of the measurement and modeled results at the 1kHz octave band in the Music Multimedia Room. The blue curve represents the measurement result, the red curve represents the simulated IR from the Image Source Method, and the yellow curve is the result from the Ray-Tracing Method.	45
4.5	Two peaks appearing in the model results are not found in the experimental results for the MMR. The blue dot in the right figures represents the speaker placed at S_1 and the red dot denotes the microphone placed at R_1 as in Table 4.3.	46

4.6	(a) Echo densities [1] of the measurement and modelled results in Fig. 4.4. The blue curve represents the measurement result, the red curve represents the simulation IR from the Image Source Method, and the yellow curve is the result from the Ray-Tracing Method. (b) Echo densities of the measurement impulse response and the modelled results by the Ray-Tracing Method with different reflection orders: second-order echo density profile (red), third-order echo density profile (yellow) and fourth order echo density profile (purple).	47
4.7	Impulse responses and echo densities in three different receiver postions. . .	48
4.8	Views of Pollack Hall and its 3D model. The blue point represents the position of the speaker S_1 , the red point represents the first position of the micropohone R_1 , the yellow point represents the second position of the microphone R_2 , the purple point denotes the third position of the microphone R_3 . All the points' coordinates are listed in Table 4.6.	50
4.9	Impulse responses and echo density curves of the measurement and modeled results at 1kHz octave band in Pollack Hall. The blue curve represents the measurement result, the red curve represents the simulation IR from the Image Source Method, and the yellow curve is the result from the Ray-Tracing Method.	52
4.10	Views of Tanna Schulich Hall and its 3D model. The blue point represents the position of the speaker S_1 , the red point represents the first position of the micropohone R_1 , the yellow point represents the second position of the microphone R_2 , the purple point denotes the third position of the microphone R_3 . All the points' coordinates are listed in Table 4.8.	54
4.11	Impulse responses and echo density curves of the measurement and modelled results at 1kHz ovtave band in the Tanna Schulich Hall. The blue curve represents the measurement result, the red curve represents the simulation IR from the Image Source Method, and the yellow curve is the result from the Ray-Tracing Method.	55
4.12	Views of the Wirth Opera Studio model. The blue point represents the position of the speaker S_1 , the red point represents the first position of the micropohone R_1 , the yellow point represents the second position of the microphone R_2 , the purple point denotes the third position of the microphone R_3 . All the point's coordinates are listed in Table 4.10.	57

4.13	Impulse responses and echo density curves of the measurement and modelled results at 1kHz octave band in the Wirth Opera Building. The blue curve represents the measurement result, the red curve represents the simulation IR from the Image Source Method, and the yellow curve is the result from the Ray-Tracing Method.	58
A.1	Details of the Music Multimedia Room model. The blue point represents the position of the speaker S_1 , the red point represents the first position of the microphone R_1 , the yellow point represents the second position of the microphone R_2 , the purple point denotes the third position of the microphone R_3 . All the points' coordinates are listed in Table 4.4.	63
A.2	Details of the Pollack Hall model. The blue point represents the position of the speaker S_1 , the red point represents the first position of the microphone R_1 , the yellow point represents the second position of the microphone R_2 , the purple point denotes the third position of the microphone R_3 . All the points' coordinates are listed in Table 4.6.	64
A.3	Details of the Tanna Schulich Hall model. The blue point represents the position of the speaker S_1 , the red point represents the first position of the microphone R_1 , the yellow point represents the second position of the microphone R_2 , the purple point denotes the third position of the microphone R_3 . All the points' coordinates are listed in Table 4.8.	65
A.4	Details of the Wirth Opera Studio model. The blue point represents the position of the speaker S_1 , the red point represents the first position of the microphone R_1 , the yellow point represents the second position of the microphone R_2 , the purple point denotes the third position of the microphone R_3 . All the points' coordinates are listed in Table 4.10.	66

List of Tables

2.1	Center frequencies of acoustic octave bands and their corresponding wavelengths.	6
2.2	Attenuation constant m at 20 degrees Celsius and standard atmosphere pressure [9]	8
4.1	Items used for room measurements	39
4.2	Physical Coefficients in Room Models	40
4.3	Material absorption coefficients in the Multimedia Room	42
4.4	Location of source S_1 and receivers R_1, R_2, R_3 in the Multimedia Room (m)	42
4.5	Material absorption coefficients in the Pollack Hall	51
4.6	Location of source S_1 and receivers R_1, R_2, R_3 in the Pollack Hall (m) . .	51
4.7	Material absorption coefficients in the Tanna Schulich Hall	53
4.8	Location of source S_1 and receivers R_1, R_2, R_3 in the Tanna Schulich Hall (m)	54
4.9	Material absorption coefficients in the Wirth Opera Studio	56
4.10	Location of source S_1 and receivers R_1, R_2, R_3 in the Wirth Opera Studio (m)	57

Chapter 1

Introduction

1.1 Motivation

When a sound is generated in a room, it quickly spreads out and interacts with the various surfaces and objects within the space, forming what is referred to as the reverberant response of the room. When the reflected wave components reach a listener, they provide cues that the human perceptual system associates with geometrical properties of a room. Such impression can help listeners distinguish if the sound is made in a cathedral or an office, in a bathroom or a living room.

Reverberation contains two parts: the early reflections and the late reflections. Early reflections include sparse waves reflected from the objects at early time. These reflections provide physical information like geometry and materials of the space. The time between two reflections will be small in a narrow space and will be longer in a larger space. Materials with less absorption leave waves with more energy to propagate and bounce while materials with strong absorption make the reverb time much shorter. Late reflections are composed of waves that have gone through several reflections orders. Tabs in this part are denser than those in the early part and seem to come from everywhere.

The amount of the reverberation in the music and sounds greatly influences the impression of the listener. A sound with appropriate reverberation can exhibit its vitality. On the other hand, a sound with weak reverberation or without reverberation will sound dry and lifeless. A sound with too much reverberation sounds too muddy, even confusing for the listeners to understand. Consequently, real sound environments such as concert halls strive for designs that produce perceptually pleasing levels of reverberation for their intended uses

[10]. In acoustic environment design, different computational models are used to predict the reverberant response of a room before it is built.

In this work, our focus is mainly on the early reflection part of the reverberation simulation. Previous model techniques assume the early reflections as idealized specular reflections, while in reality many surfaces are not smooth nor flat, producing nonspecular components at each reflection. This thesis is motivated by the following question: How realistic is the assumed specularity of early reflections and can we assess this using room impulse response measurements? To conduct this research, it is necessary to model sound propagation in rooms of different geometries and compare the simulations to the measurements. We then investigate the use of a computable property of room impulse responses called echo density [1] to quantify specularity.

1.2 Outline

The thesis is organized as the following structure:

Chapter 2 first gives a background of basic acoustics used in the thesis. Also, two geometric acoustic techniques are introduced: the Image Source Method (ISM) and the Ray-Tracing Method. Commercial acoustic softwares based on two methods are presented in the last part of the chapter.

Chapter 3 deals with the implementation of the two GA models in 3D rooms, including the model initialization, acoustic model building, sound path establishing and testing, and energy recording. Similarities and differences between the Image Source Method and the Ray-Tracing Method are compared in detail and a parameter evaluating echo densities in the impulse responses is also introduced.

Chapter 4 presents the measurement method and results of four real rooms in Schulich School of Music, including two studios and two concert halls. The measured impulse responses are then compared with corresponding results made by computational simulations in 3D models. Analysis of the diffuse effects in each room based on room geometry and acoustic modeling is mainly presented in this chapter.

Chapter 5 gives a summary of the results and concludes the work. Further improvements will also be suggested in this chapter.

1.3 Contributions

In music production, different artificial reverberations are added to sounds to improve the spatial hierarchy. There are two main types of the reverberation plugins according to generation methods: the algorithm reverberation plugins and the convolution reverberation plugins. It is convenient to adjust parameters such as the reverberation time and degree of diffusion in algorithm plugins, but the early reflections sound unrealistic and are not compatible with the other sound in the field. Convolution reverberation plugins have better performance in the early reflections as they use real impulse responses, but it is hard to adjust other parameters. Excessive adjustment or processing of recorded impulse responses will result in distortion of the original impulse responses and render the processed sounds unnatural. This work provides a new method that can help designers find appropriate early reflections basing on real room acoustics and improve the sound quality of the reverberation plugins. In room acoustics' design, reverberations are regarded as an essential factor in the evaluation of room's acoustic properties. Improvements of the early reverberation computation will contribute to the accuracy in the room acoustic design. Other fields like speech cognition and environment science might also take advantages of research on early reverberation simulation.

Chapter 2

Geometric Acoustic Techniques

Geometric acoustic (GA) techniques have been a popular way to design concert halls or to analyze acoustic conditions [6]. They provide efficient methods of solving practical acoustic problems with rooms containing non-rigid walls and complicated shapes. Furthermore, computer simulations based on GA are cheaper and faster than those of traditional acoustic methods that involve solving the wave equation. Digital simulation of GA was first introduced by Schroeder et al. [11]. After that, this method has been used in many problems in room acoustics. Krokstad et al. were the first authors who used computational simulations to analyze concert halls [12]. In their works, various acoustical parameters are extracted from impulse responses modeled by Ray-Tracing Method. Other analyses on environments like factories also utilize this method as a reliable reference [13–15]. The following sections will introduce fundamental geometric acoustics. Two main techniques widely used in GA are explained. The first one is called the Image Source Method (ISM) and the second one is referred to as the Ray-Tracing Method [16]. Commercial applications of the models and their extensions will be discussed in the last part of the chapter.

2.1 Basic Geometric Acoustics

2.1.1 Wave Propagation

This section introduces the basic propagation behaviors of sound travelling in rooms. Sound is wave motion within matter, in forms of gaseous, liquid or solid, and it exhibits, in many respects but not in all, behaviors similar to other wave motions encountered in nature, i.e.

water waves and light waves [17]. In sound waves, the air being the medium of interest in room acoustics, the disturbance is an alteration of the atmospheric pressure over and under its mean value, which produces a back-and-forth movement of the air molecules along the direction of propagation[18]. These waves are longitudinal waves, as opposed to water waves, which are an example of transverse waves.

The propagation of the sound in air is illustrated in Fig. 2.1. The upper part is the atmospheric pressure and the lower part illustrates the motion of the air molecules associated with the propagation of sound. The gradient of the pressure increases with the growth of sound intensity.

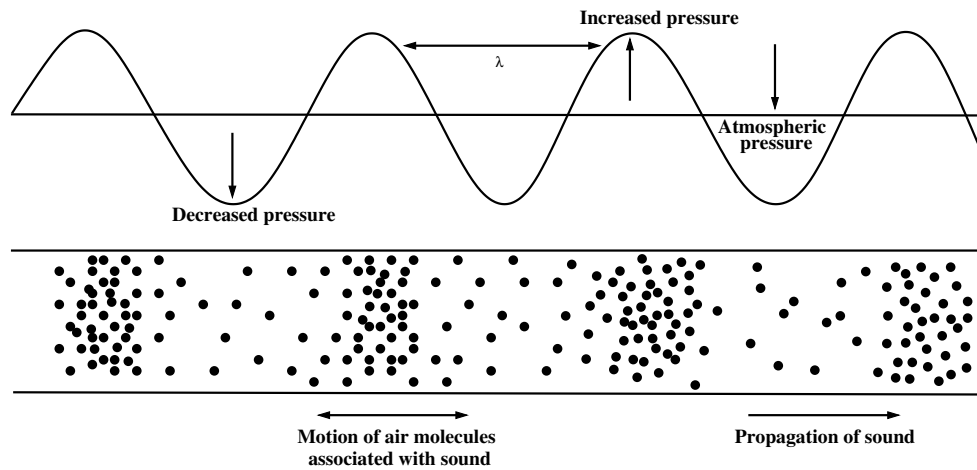


Fig. 2.1 Sound propagation through the air (based on [2]).

The velocity of sound waves in air is independent of the wave size, and it doesn't have an electromagnetic nature as in the case with light. If the medium is assumed to be homogeneous and at rest, the speed of sound is constant in space and time [4] and the velocity can be expressed as the following equation for air:

$$c = (331.4 + 0.6\Theta) \quad [m/s] \quad (2.1)$$

where Θ is the temperature in centigrade.

When evaluating the frequency response of sounds in rooms, it is common to consider frequency ranges called octave bands [19]. Two sound frequencies f_1 and f_2 , with a relation $f_1/f_2 = 2$, make up an interval that has a frequency bandwidth of $\Delta f = f_2 - f_1$. Table

2.1 gives the central frequencies of the acoustic octave bands. Below the central frequencies are the corresponding wavelengths. Filters can be used to analyze signals within specific octave bands.

Table 2.1 Center frequencies of acoustic octave bands and their corresponding wavelengths.

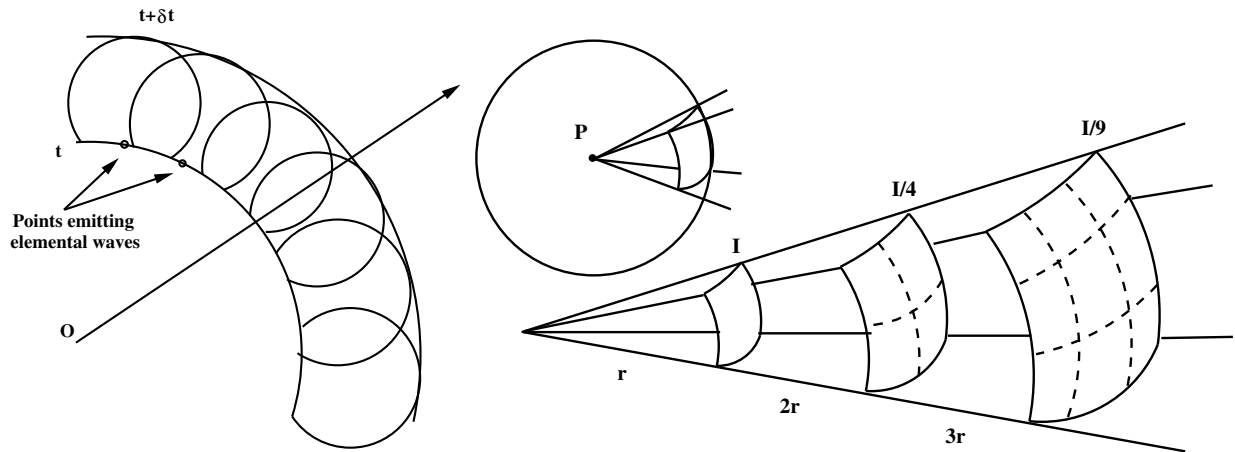
$f[Hz]$	63	125	250	500	1000	2000	4000	8000
$\lambda[m]$	5.302	2.672	1.336	0.668	0.334	0.167	0.084	0.042

Sound propagation is usually described by the Helmholtz equation as given by Eq. 2.2, where p denotes the sound pressure, and x, y, z represent the Cartesian coordinates. The problem with the wave equation is that its solution does not always exist in an analytic form [20], and therefore sometimes requires approximations.

$$c^2 \Delta p = c^2 \left(\frac{\partial^2 p}{\partial x^2} + \frac{\partial^2 p}{\partial y^2} + \frac{\partial^2 p}{\partial z^2} \right) = \frac{\partial^2 p}{\partial t^2} \quad (2.2)$$

In geometric acoustics, however, the traditional theory of sound fields is simplified to an abstraction like optics behaviours. In such situations, waves are usually limited to high-frequencies. This means that the wavelength of the sound must be small enough compared to the dimensions of the room, or else other wave phenomena begin to have an impact on the accuracy of calculation. A wave at a frequency of 1000Hz has a wavelength around 0.34m at normal room temperature. This length is small enough compared with the regular room dimensions, making the assumption applicable. In such conditions, waves can be viewed as rays traveling in a particular direction, subject to the laws of propagation like a light ray [4]. Moreover, diffraction and interference properties of waves are neglected in GA.

Huygens propagation principle can be used to explain sound propagation in air. In this theory, every point on that wavefront produces elemental spherical waves. These elementary waves construct another wavefront after a time interval Δt , as shown in Fig. 2.2a. In this way, each source point spreads its energy in all directions without limit, the total energy of the rays falls proportionally to $1/r^2$ where r is the distance from the source point to the wavefront. This is also called the divergence law. Figure 2.2b illustrates the law, where the sound intensity I at a given distance r is expressed as the sound power W divided by the surface area of the sphere [7]. From the formula, it is evident that the energy decays as the distance increases, regardless of the sound velocity.



(a) The Propagation of wave fronts in Huygens principle (based on [3]).

(b) Divergence law for sound propagation (based on [3]).

$$I = \frac{W}{4\pi r^2} \quad (2.3)$$

2.1.2 Sound Absorption

This section describes the energy transformations of sound propagating in rooms. When traveling long distances, part of the energy in a rays is absorbed because of losses inherent in the medium impedance. The sound power decays exponentially with the distance, which can be expressed as follows:

$$P = P e^{-mx} \quad (2.4)$$

where m is the medium coefficient determined by the medium type and x represents the distance of the ray path. Table 2.2 gives some typical values for air [9]. Note that the dependence of air absorption on temperature is weak [21].

Sound energy is also absorbed when incident waves reflect off boundaries of the room. The new direction after the reflection is determined by Snell's reflection law, as illustrated in Fig. 2.3. The angle between the incident ray and the normal to the reflecting plane must be equal to the angle between the reflected ray and the normal to the reflecting plane. This law can be written as the following vector expression:

Table 2.2 Attenuation constant m at 20 degrees Celsius and standard atmosphere pressure [9]

Relative Humidity	Frequency in Hz			
	1000	2000	3000	4000
40	0.0013	0.0037	0.0069	0.0242
50	0.0013	0.0027	0.0060	0.0207
60	0.0013	0.0027	0.0055	0.0169
70	0.0013	0.0027	0.0050	0.0145

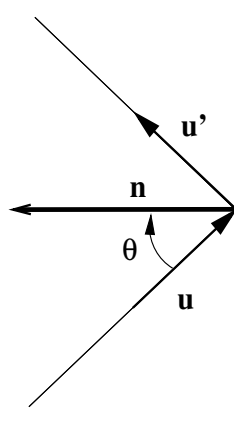


Fig. 2.3 General reflection process.

$$u' = u - 2(u \cdot n) \quad (2.5)$$

where u and u' are unit vectors representing the direction of the incident and the reflecting rays, n denotes the normal to the reflecting plane. During the reflection, part of the energy is absorbed by the wall. The absorption coefficient of the plane-wave reflection can be expressed as:

$$R(\theta) = \frac{Z_s \cos \theta - \rho c}{Z_s \cos \theta + \rho c} \quad (2.6)$$

where Z_s is the impedance of the surface, theta is the incident angle and ρc represents the air impedance. However, in practice it is common to use the absorption coefficient α in

computations:

$$\alpha(\theta) = 1 - |R(\theta)|^2 \quad (2.7)$$

In this simplification, phases of the reflections are entirely neglected. In this work, absorption coefficients are independent of angle. In other words, the incident angle of the ray does not influence the wall absorption value.

2.1.3 Sound Diffusion

When interacting with the walls, not all parts of a sound wave are specularly reflected. This may be caused by the finite size of the wall or by the unevenness of the walls surface geometry and/or impedance [22]. These non-specular reflections, usually called diffuse reflections, have a great importance in accuracy of acoustic modeling. Two ways are commonly used to realize the diffuse reflections. First, the sound waves can be divided into two parts at each reflection: a pure specular wave and many diffuse waves. The diffuse components can be determined by the scattering coefficients of the walls and by random numbers to denote the new propagating directions. The second method provides a more proficient way to implement the diffusion phenomenon. Instead of generating new waves, it maintains a single wave but letting it travel in a random direction if the reflection is a diffuse reflection. Otherwise, the reflection is specular. Though these methods are based on the diffuse-reflection coefficients of the walls, it remains unclear how these coefficients should be determined, and what are their typical values for common wall surfaces [22]. Another method for scattering was published by Mehta and Mulholland, basing on the distance between intersection points and edges of the walls [23]. Christensen and Rindel utilized the specular reflection strength to obtain a high-pass filter effect in rendering scattering [24].

In this work, the modeling of the diffusion effect is neglected for better comparison between specular components and non-specular ones.

2.1.4 The Impulse Response

This section presents how to express the room acoustic characteristics. The primary simulation results representing the room acoustic characteristics are expressed as an impulse response (IR), which is also sometimes referred to as an echogram. Figure 2.4 shows an

example of a room impulse response. Generally, it is a collection of energy peaks from different sound rays reaching a listener after varying amount of reflections. The time delays depend on the traveled paths, and the pressure intensities depend on the air absorption and the absorption coefficients of the walls involved in the propagation. According to the time clock and the energy distribution, the impulse response is divided into three parts: the direct sound, the early reflections, and the late reflections. The first impulse is always the direct sound, followed by several distinct peaks representing the early reflections. In the early part, peaks are always sparsely arrayed with energies that are relatively higher than those in the following part of the reverberation. Therefore, early paths from different direc-

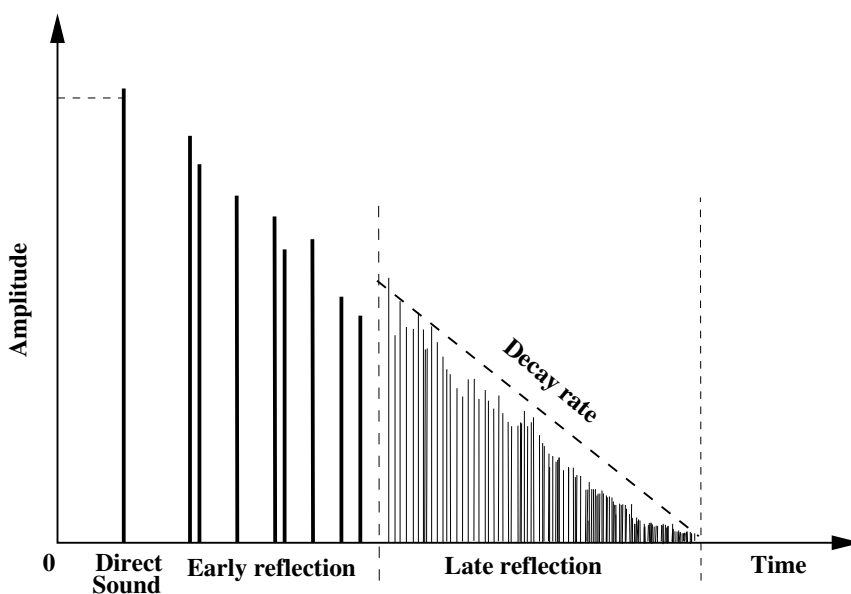


Fig. 2.4 Impulse response of a room representing the propagation of sound pressure from a source to a receiver (based on [3]).

tions can be easily observed, although sometimes background noises and overlapping peaks can complicate the task. In the late reflections part, peaks become denser along with the energy decay, which is caused by many factors. Since most reflecting surfaces in real rooms are not completely flat, waves hitting such surfaces can be reflected in many directions at the same time. This non-specular behaviour will quickly produce very dense reverberant responses. In this way, additional sound rays are generated by the reflections, which is the reason for the density increase in the late reverberation. Meanwhile, the longer the distance a sound wave travels, the more reflections with surfaces before reaching a listener, causing

more energy loss and scattering.

Impulse responses provide a lot of information about a room's sonic characteristics. Many acoustic parameters are calculated from the IR. Another important point is that auralization is obtained by processing auralized signals in the form of an impulse response. Details about auralization implementation are listed in Ref. [25, 26].

2.1.5 Acoustic levels

Sound levels are usually expressed in logarithmic scales, as the human auditory system is sensitive to an extremely large range of pressures or intensities [4]. The unit of the sound level is expressed in decibels, abbreviated as dB. The level is shown by the magnitude of a signal over a reference in the logarithm. The acoustic power level L_w is:

$$L_w = 10 \log \left(\frac{W}{W_0} \right) \quad \text{where } W_0 = 1 \times 10^{-12} W \quad (2.8)$$

The acoustic intensity level L_I is:

$$L_I = 10 \log \left(\frac{I}{I_0} \right) \quad \text{where } I_0 = 1 \times 10^{-12} W/m^2 \quad (2.9)$$

The acoustic pressure level L_P is:

$$L_P = 20 \log \left(\frac{p}{p_0} \right) \quad \text{where } p_0 = 20 \mu Pa \quad (2.10)$$

The addition of two levels, i.e. L_{I1} and L_{I2} , are determined by either adding levels in dB or solving Eq. (2.9) with intensities I_1 and I_2 .

$$I_1 = I_0 \cdot 10^{0.1L_{I1}} \quad (2.11)$$

$$I_2 = I_0 \cdot 10^{0.1L_{I2}} \quad (2.12)$$

$$I_T = I_1 + I_2 = I_0(10^{0.1L_{I1}} + 10^{0.1L_{I2}}) \quad (2.13)$$

$$L_{IT} = 10 \log \frac{I_T}{I_0} = 10 \log(10^{0.1L_{I1}} + 10^{0.1L_{I2}}) \quad (2.14)$$

$$(2.15)$$

2.2 The Image Source Method (ISM)

Carslaw first proposed the principles of the Image Source Method in 1899 [27]. Studies at that time were limited to canonical problems. Later in 1948, the research of this method in a closed cube was first presented by Cremer [28]. Afterward, in 1950, Mintzer published a similar study on the calculation of sound pressure in a rectangular room as a function of time [28]. Gibbs and Jones [29] implemented the first simulation with the method on computers. Then Allen and Berkley released a similar implementation with FORTRAN for the impulse response calculation [30]. Hereafter, Aretz et al. proved that the Image Source Method could accurately simulate the low-frequency band when using the compound angular-dependent reflection coefficients [31], which is more detailed than the previous work by Lam [32].

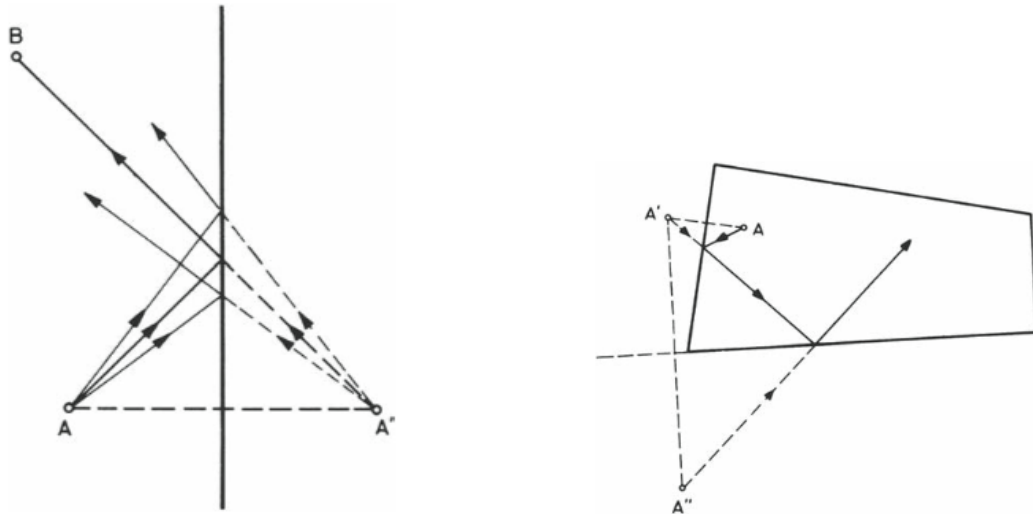


Fig. 2.5 (a) Graph interpreting the Image Source Method (from [4]). (b) Building the second order ray path (from [4]).

The Image Source Method is based on specular reflections in the spaces. The main idea of the method can be explained through Fig. 2.5(a). The sound source A is put in front of a plane. The reflected rays from the source can be regarded as emitted rays propagating from the image source A' , which has the same distance from the source to the wall but lies on the opposite side. The line linking the two sources is perpendicular to the wall plane. If B denotes the receiving point, the reflection path can be established by simply connecting the

image source and the receiver. However, more tests should be taken to prove the validity of the path. These tests should include testing whether the path is in the boundary of the wall and whether there exist obstructions in the path. Detailed discussions of these tests will be provided in the next chapter. When the reflected ray collides with another wall, the next image source can be constructed by mirroring the first image source A' to A'' through the second wall plane, as illustrated in Fig. 2.5(b). Higher orders of image sources are obtained by continuing the process repeatedly. According to the replication of the imaging process, if a room has N walls, the number of image sources constructed on the i th order will be $N(N - 1)^{(i-1)}$, and the total image sources built will be the sum of all the image sources:

$$N(i_0) = N \frac{(N - 1)^{i_0} - 1}{N - 2} \quad (2.16)$$

Some energy will be absorbed by the walls after the reflections. Usually, the amount of energy absorbed is calculated through the wall absorption coefficients α as mentioned in the previous section. Although α is angle dependent and the angles are known in the simulation, it is common to use a unified value as the absorption coefficient for the wall because of the lack of angle-dependent absorption data for wall materials.

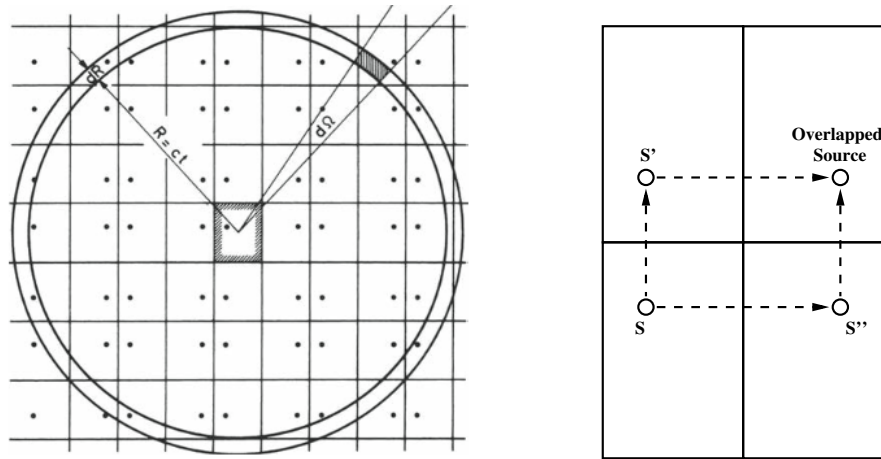


Fig. 2.6 (a) The distribution of image sources in a rectangular room (from [5]). (b) An example of an overlapped image source building.

A classical example in mapping the image sources is shown in Fig. 2.6(a). Here a 2D map is shown with some image sources built along with the room frames. Because the room is rectangular, the image sources demonstrate a high regularity in their distribution.

The four squares adjacent to the original one represent the environment of the first order sources while squares close to the first order sources are second order images and so on. The source building can go infinitely if no conditions limit the image numbers. If $X = (x, y, z)$ is the position of the source, the positions of the other image sources can be written as the following expression:

$$X' = (\pm x + 2nL_x, \pm y + 2lL_y, \pm z + 2mL_z) \quad (2.17)$$

where n , l and m are integer parameters determined by the exact positions of the source points; L_x , L_y and L_z represent the room dimensions. All the sources in the mapping are valid because of the simplicity of the room geometry. Note, however, that there can be overlapping image sources. Using Fig. 2.6(b) as an example, the source mirrored by the north wall and then the east wall will overlap the source mirrored first by the east wall and then by the north wall. Eq. (2.17) is only valid for rectangular room shapes. For rooms with irregular shapes, each image source should be built according to the exact position of each wall.

After all the valid sources are found and positioned, the impulse response can be generated by assuming that all these sources send rays to the receiver at the same time. Different positions of sources lead to different time delays and the different levels of attenuation. The time of the energy peak of a ray is determined by the distance from the image source to the receiver. Low-order sources with small distances take less time to reach the receiver, high-order sources at large distances from the original source will take longer to arrive at the listener position. The remaining strength should include the wall absorption process represented by the intersection points between the sound paths and the walls crossed by the path. If the absorption coefficients of all walls are frequency independent, the general expression of an impulse response can be written as:

$$g(t) = \sum_n A_n \delta(t - t_n) \quad (2.18)$$

where A_n is the strength of a particular source response, t_n is the exact time that a source reaches the receiver.

2.3 The Ray-Tracing Method

Early research on the Ray-Tracing Method dates back to 1958 when Allred and Newhouse studied the mean free path length calculation [33]. However, the real 3D simulation of the Ray-Tracing Method was implemented by Krokstad et al. in 1968 [12]. Then, Schroeder published a similar model in 2D enclosures in 1970 [34]. As computers became more and more powerful, the technique gained in popularity for visual spaces simulations. This is not restricted to acoustic field simulations, and has been extended to other fields like computer graphics, aerospace engineering, marine science and so on.

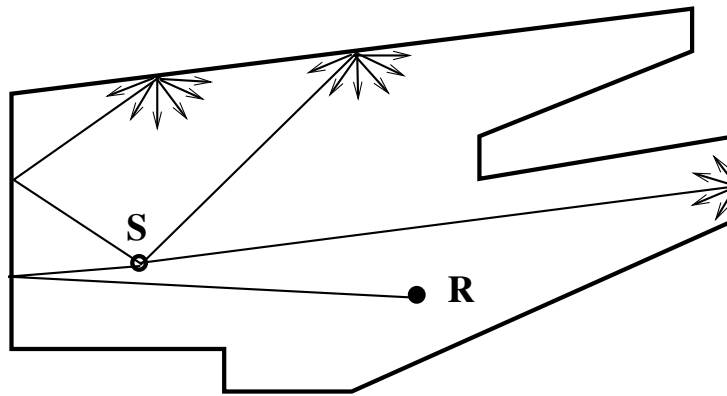


Fig. 2.7 The principle of the ray tracing technique (based on [6]).

The principle of the Ray-Tracing Method is shown as shown in Fig. 2.7. A sound source S is assumed to send many rays with different directions into a room. These rays travel in straight lines in the room with specific energies, bouncing off the walls and changing their directions. During propagation, the energy of each ray will be lost at each reflection with walls and medium absorption mentioned in the previous section. The receiver counts and records energy and timing information to form the impulse response of the room. To terminate time-consuming rays in a simulation, a limitation is usually set to truncate them. The criterion can be the smallest sound energy e_{min} needed, the maximum reflection order n_{max} required or a maximum simulation time t_{max} . In practice, the ray tracing process is computed ray by ray. One ray starts tracing after the previous ray is detected by the receiver or reaches the limit condition in the program. Due to the frequency dependence of the absorption, the whole process must be repeated in different frequency bands. The flow

diagram is shown in Fig. 2.8.

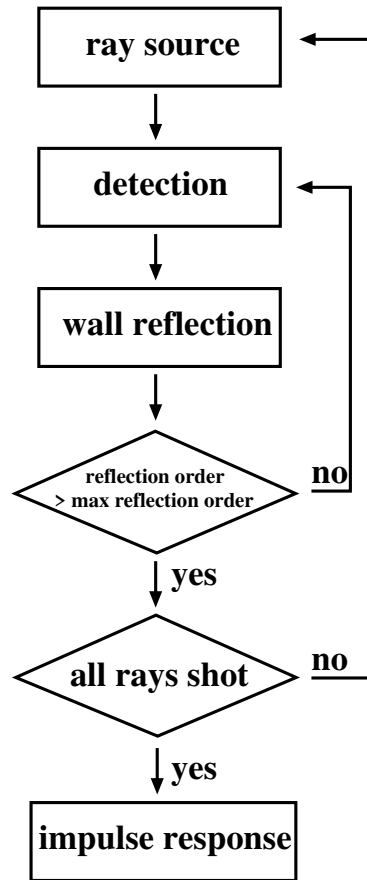


Fig. 2.8 The flow diagram of the ray tracing algorithm (based on [7]).

Another method of terminating the propagation rays is to apply “Russian Roulette” [35]. This method assumes that each ray has a probability to be annihilated on each reflection. The probability is based on the absorption coefficient of each wall. The weakness of this method, however, is that it cannot be implemented in different octave bands. And it is also more computationally demanding than the previous method.

Most of the processings in the Ray-Tracing Method is concerned with determining which plane rays are going to hit and testing if the intersection points are inside the wall boundaries. These tests are identical to the tests in the Image Source Method. In the tests, the polygon, the normal of the wall and the direction vector of the ray are combined to check the validity of the collision. If the path is valid after the polygon test, wall absorption

will be processed, and a new direction is generated according to the specular reflection law.

One factor differentiating the Ray-Tracing Method from the Image Source Method is the number of rays emitted and their predetermined initial directions before emission. The initial ray number plays an important role in the simulation time as well as in the simulation accuracy. In practice, room geometry and wall materials affect the appropriate ray number chosen, as studied by Vorlander [35]. Another method published by Kulowski [36], suggests checking the credibility by calculating the standard deviation among different runs. In his research for large ray population, the absolute differences between two different runs of reverberant responses are first calculated. Then means of differences are computed to show the stability of the impulse responses under the selected ray number. An optimal initial ray number should cost the least time while maintaining the stability of the simulation results in an accurate region.

Ideally, the receivers in the Ray-Tracing Method should be “point like,” as in the image source model, but the chance of a ray intersecting such a small target will be very small. As a result, the receiver is defined to have a finite volume. To avoid angle-dependent cross sections, the shape of the receiver is usually a sphere with a cross-section S_{sphere} :

$$S_{sphere} = \pi r_d^2 \quad (2.19)$$

where r_d is the radius of the sphere. Whenever a ray has a new direction, a test should be run to check if the ray will travel “into the sphere”. This test is performed by calculating the perpendicular line between the center point of the receiver, which corresponds to an omnidirectional headphone, and the tracing line, comparing the distance of the line with the sphere radius r_d to see if the distance is smaller than r_d .

The size of the sphere in the model is studied and analyzed by Vorlander [37] in 1989, who mentioned a relationship between the initial ray number N , the time the ray spent in the air t and the receiver’s radius r_k :

$$N_{min} = 4(ct_{max})^2/r_k^2 \quad (2.20)$$

where c is the sound speed. Then Lehnert [38] published another method to calculate the receiver radius:

$$r_k = ct\sqrt{\frac{2\pi}{N}} \quad (2.21)$$

Later, Zeng Xiangyang et al. [39] put forth a new model considering the source-to-receiver distance d_{SR} , the initial ray number N and the sound space volume V :

$$r_k = \log_{10}(V) \cdot d_{SR} \cdot \sqrt{\frac{4}{N}} \quad (2.22)$$

It is demonstrated in Chapter 3 that Vorlander's model gives the most accurate results in predicting the receiver size regarding the initial ray numbers.

2.4 Related Applications

Geometric acoustics techniques have been used in commercial software to simulate and analyze sound environments. In these products, the Image Source Method and the Ray-Tracing Method are the primary models. Additional algorithms are built to accelerate the modeling process, including a combination of two models. In this thesis, two software are introduced: Odeon and Catt-acoustic.

2.4.1 Odeon

Odeon selected the Ray-Tracing Method as the starting model for room acoustic simulations. In 1989, a hybrid model was introduced in Odeon to accommodate both Ray-Tracing Method and the Image Source Method, combining the best features of both approaches [40, 41]. Ray-tracing is used in early reflection tests of image sources to filter out irrelevant sources, saving computation time. Later in 1992, another method called the secondary source method was implemented for more accurate calculations of the late portions of a reverberant response. Then in 1995, the vector based scattering method was applied to combine diffuse and specular reflections during the ray-tracing, which also makes improvements in model efficiency.

2.4.2 Catt-Acoustic

Catt-Acoustic is another Windows-based acoustics software system that supports room acoustics prediction and auralization in mono, stereo, binaural and B-format styles. The

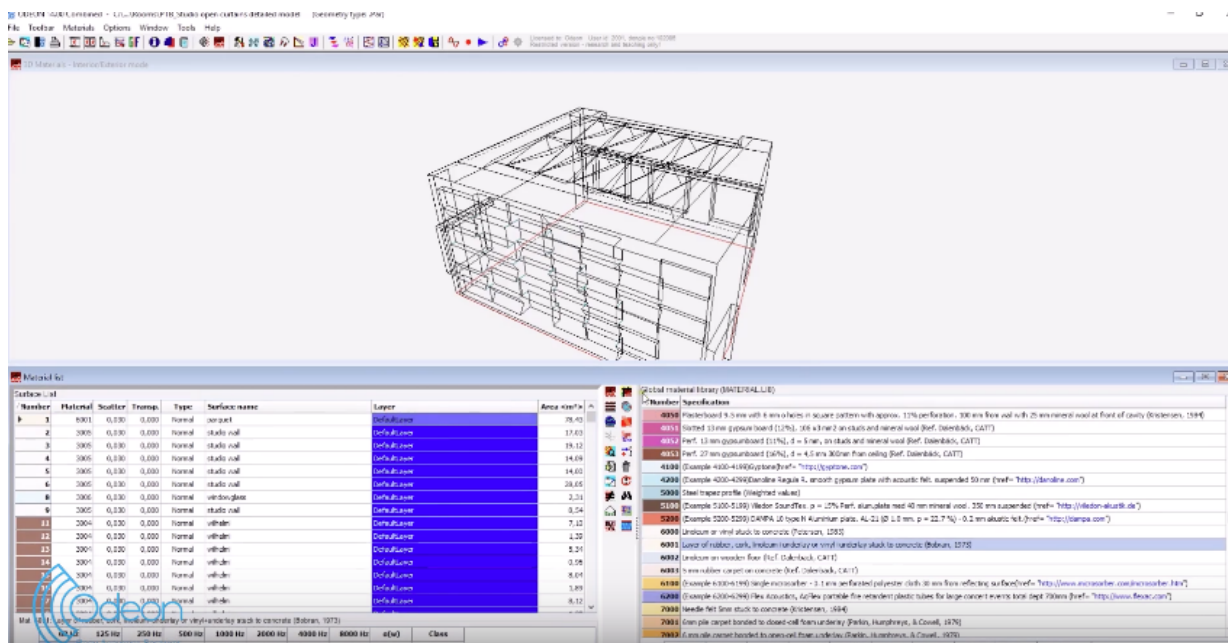


Fig. 2.9 Odeon acoustics simulation software.

model in the software applies approximate cone-tracing where rays are changed into cones whose apex is the origin and the angle between the central line and the cone boundary is the spread angle [42]. In the cone-tracing method diffuse reflection is handled by split-up of cones striking diffusing surfaces [43]. The algorithm improves the “brute force” process of cone split-up by utilizing the properties in diffuse reflections. Reflection growth extrapolation is then used to decrease the number of secondary cones, improving the efficiency of calculation. The model in the software is especially suitable for auralization since a lot of diffuse reflections are created to smooth the reverberation.

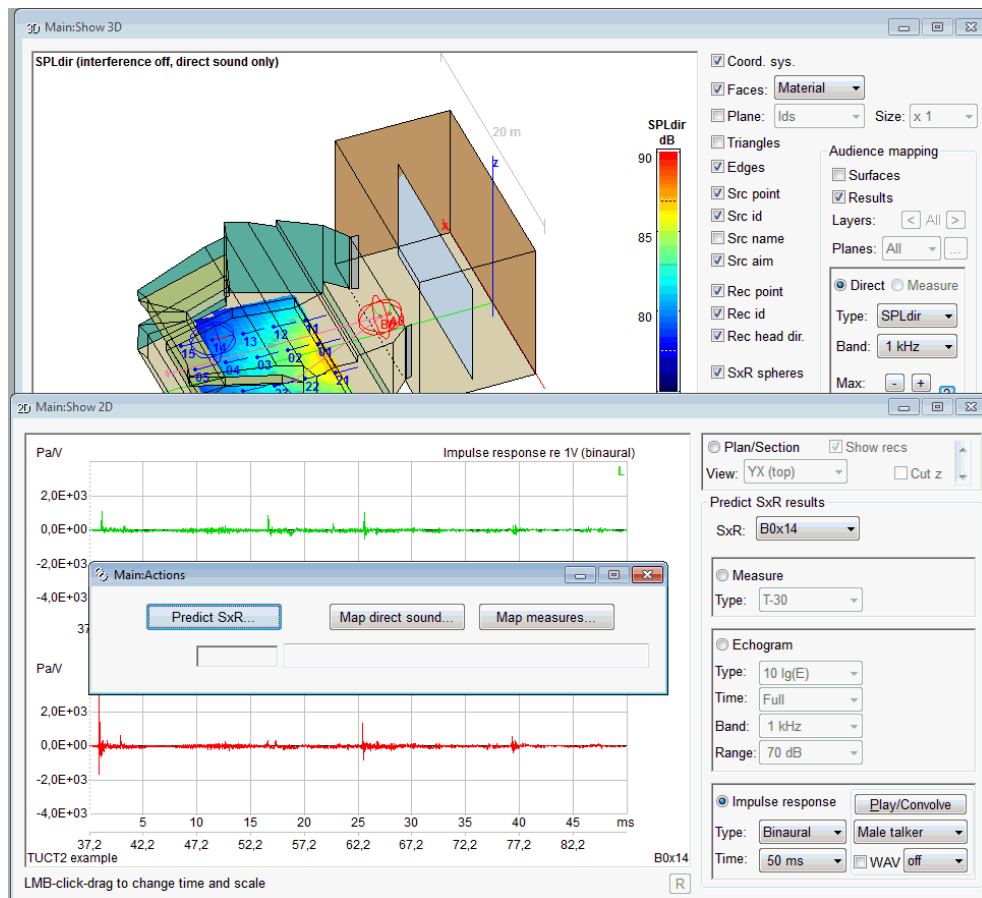


Fig. 2.10 Catt-Acoustics acoustics simulation software.

Chapter 3

Model Implementation in 3D Enclosures

In this chapter, the implementations of two models, the Image Source Method, and the Ray-Tracing Method are presented in 3D enclosures. Two main parts are involved in the discussion of the Image Source Method building: the geometrical part and the energetic part. Descriptions including the surface properties and locations of the source and receiver of the virtual rooms will be given in the geometric part. The source imaging process and path validity detection methods will also be discussed. In the second part, I analyze the methods used for obtaining the energy of every ray as well as forming the impulse responses. In the Ray-Tracing Method, most parts of the model are identical to the elements in the image-source method, and additional aspects including initializing the ray directions and detecting the arriving rays are discussed. At the end of the chapter, an echo density calculation is introduced as a way to potentially characterize the relative sparseness of reflections in an impulse response [1].

3.1 Image Source Method Modeling

3.1.1 Digital Constructions of Rooms

In general, the process of geometrical simulation can be described as the interactions between the sound paths and the room walls. In Cartesian coordinates, a sound path in a 3D enclosure is interpreted as a line with the following equation:

$$\frac{x - x_1}{l} = \frac{y - y_1}{m} = \frac{z - z_1}{n} \quad (3.1)$$

where (x_1, y_1, z_1) represents the coordinates of a point in the path line and $\vec{n}_l(l, m, n)$ represents the vector pointing to the lines direction. A wall in a room can be represented as a plane written as the following equation:

$$Ax + By + Cz + D = 0 \quad (3.2)$$

The first three numbers A , B and C constitute the norm vector $\vec{n}_p(A, B, C)$ which is orthogonal to the plane. Coefficient D restricts the exact plane position. As shown in Fig. 3.1, the plane equation can be calculated from three non-collinear points on the plane. All the walls in a room are saved in the form of the above equation. Here two restrictions on each plane should be noted. For the first one, the expression represents an infinite plane in a room while real room walls have borders, which is one of the reasons for the necessity of “visibility” tests. Secondly, the direction of the normal on a plane distinguishes the

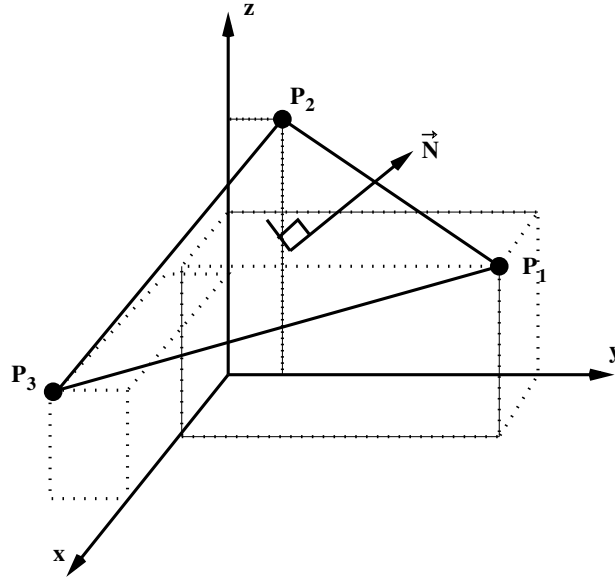


Fig. 3.1 A plane obtained from three points (based on [3]).

inside and the outside of that plane. As most calculations and tests are related to the angle between the vector of the ray path and the norm of the wall, the exact norm directions

should be determined according to the geometrical structure of the room. Thus, the points on each wall must be saved in a particular order for further calculations. This procedure is useful in the validity tests introduced in the following section.

3.1.2 Source Imaging Process

Most studies about the Image Source Method simplify the geometrical structure to rectangular rooms. Due to the symmetrical properties of such rooms, the topology of image sources can be quickly built with Eq. (2.17) even without the plane equations. In rooms with asymmetrical shapes, however, there are no guaranteed regularities among the walls, and every image source's position only depends on the position of the corresponding mirror wall. Thus the geometrical information of each wall cannot be neglected when doing image processing in an arbitrary room.

The basic method to generate image sources can be written as the following formula:

$$\begin{bmatrix} x' \\ y' \\ z' \end{bmatrix} = \begin{bmatrix} x \\ y \\ z \end{bmatrix} - 2 \frac{xA + yB + zC + D}{A^2 + B^2 + C^2} \begin{bmatrix} A \\ B \\ C \end{bmatrix} \quad (3.3)$$

where A , B , C and D are coefficients of the mirror plane function, (x, y, z) are the coordinates of the source point and (x', y', z') denotes the coordinates of the image source point.

Another image process is proposed by Lee [8]. In this method, a transformation matrix $[T]$ is used to obtain a new image coordinate system from the origin coordinates. The source point S' should be multiplied by cascades of the wall transforming matrices to obtain a new image source:

$$S' = S[T_1][T_2] \dots [T_n] \quad (3.4)$$

where n equals the matrix number by which the source should be multiplied. However, once a new coordinate system is built, other information such as the plane functions should also be updated to the new system. Thus, a new set of transforming matrixes for planes should be built in every imaging process, making the method complicated to compute.

The image process used in this work is the Gram-Schmidt algorithm. The principle of the algorithm is shown in Fig. 3.2. A vector v is formed by linking the source S and one

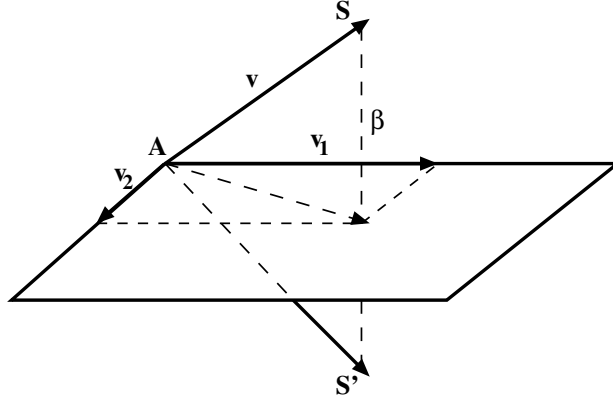


Fig. 3.2 An image source obtained with Gram-Schmidt algorithm.

vertex A on the mirroring plane. The vector is then projected onto the plane's orthogonal basis to v_1 and v_2 . The projection of the vector β on the plane normal is obtained from the vector subtraction $v - (v_1 + v_2)$. The image point S' then can be written as:

$$S' = v - 2\beta + A \quad (3.5)$$

3.1.3 Path Validity Detection

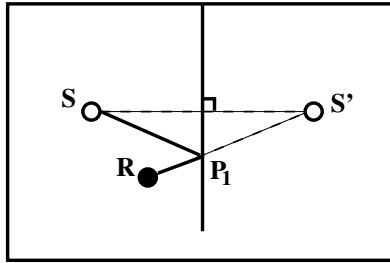
The intersection point (x_P, y_P, z_P) , between a line Eq. (3.1) and a plane Eq. (3.2) is calculated as the following equation:

$$\begin{bmatrix} x_P \\ y_P \\ z_P \end{bmatrix} = \begin{bmatrix} x_1 \\ y_1 \\ z_1 \end{bmatrix} - \frac{x_1 A + y_1 B + z_1 C + D}{lA + mB + nC} \begin{bmatrix} l \\ m \\ n \end{bmatrix} \quad (3.6)$$

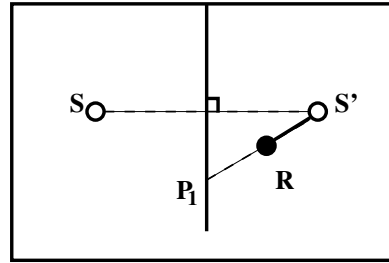
In reality, every plane has its boundaries, and every ray path has its endpoints. These restrictions are not reflected in the mathematical equations. As a result, additional tests should be implemented to check the validity of the imaged source. The following section will discuss each category of tests and the algorithm extending these tests to high order reflection paths.

a. In-path Test

Paths in the Image Source Method can be represented by virtual lines between the image sources and the receivers. As we can see in Fig. 3.3a, a sound source is emitting a sound ray through one reflection of an intruding wall in the room. If the receiver point R and the first order image point S' are linked together, we can obtain the intersection point P_1 on the reflecting surface. Segment $\overline{S'P_1}$ can be regarded as the mirror path from the source S to P_1 . We should notice that P_1 lies exactly on the virtual path $\overline{S'R}$. The straight line



(a) A valid first order reflection path.



(b) An invalid first order reflection path.

Fig. 3.3 In-path test on the image source. S denotes to the original sound source, S' is one image source of S , R represents the receiver, the intruding wall is the reflecting surface, and P is the intersection point. The path in b is invalid due to the position of the intersection point lying out of the path.

equation, however, is mathematically infinite in length as written in Eq. (3.1). This property makes the intersection points calculated from the virtual paths, and the reflecting surfaces, sometimes stand on the extended lines of the paths, as shown in Fig. 3.3b. Obviously, the path constructed is invalid in this case since it is impossible to send a ray reflected by the intruding wall from the source to the receiver, so the paths are unavailable if the intersection points is located on an extension of the virtual path. However, such paths can pass the in-polygon test and the visibility test introduced in the following section. As a result, we must ensure that the intersection point lies between the two endpoints of the virtual path after every imaging process. The test consists of computing the inner product of vector $\overrightarrow{P_1R}$ and $\overrightarrow{P_1S'}$ and deleted paths if the result is positive.

b. In-polygon Test

The in-polygon test is mainly performed in a two-dimensional domain. There are many ways of performing the test. One method is to form vectors from the intersection point to each of the vertices of the outer boundary of the room [5]. Then cross products of successive vectors which are all orthogonal to the plane are computed. If these products all point to the same side, the intersection point is inside the polygon. Otherwise, the point is out of the polygon boundary, indicating the path is invalid. While this method is a straightforward and efficient way of testing the path's validity, it is only available when all the inner angles of the polygon are less than 180° . A counter example is shown in Fig. 3.4. The algorithm is run to test if the intersection point P is in the polygon of the reflecting surface ABCDEF and successive products starting from vector \vec{PA} to vector \vec{PF} are calculated. All the angles between two vectors rotate anticlockwise except the one between vector \vec{PB} and \vec{PC} which is clockwise. This is because inner angle $\angle CDE$ is larger than 180° , which causes the cross product of vector \vec{PB} and \vec{PC} to have the opposite sign from the other cross products. In this case, the algorithm incorrectly identifies the point as being outside the polygon. This problem can be solved by dividing the polygon into several small polygons whose inner angles are all less than 180° .

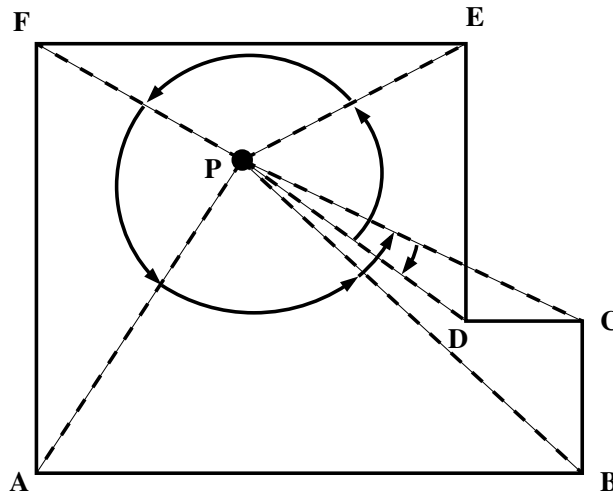


Fig. 3.4 The in-polygon test in ISM algorithm.

Another alternative algorithm can solve the inner angle problem. Instead of calculating the cross products, angles between two successive vectors formed by the intersection point

and polygon vertices are computed. If the point is in the polygon, the sum of these angles is equal to 2π . Otherwise, the sum equals 0. The new algorithm guarantees the accuracy of the in-polygon test in all kinds of polygons but adds more burdens on computation. In the first method, the test can stop as soon as there exists a product that points to an opposite side. In contrast, in the second algorithm, all the angles between intersection points and vertices must be calculated before a final decision can be made. In this paper, we choose the second method considering the complexity of the geometrical structure of measured rooms.

c. Visibility Test

Here we combine the two test algorithms above to determine if there is any obstruction in the sound path. Fig. 3.5 gives an example of such an invalid path. Although the collision point P_1 is in the boundaries of the reflection wall, another wall blocks the path $\overline{RP_1}$, making the path invalid. The test should be run for all the other walls in the simulation that the ray is not determined to have reflected from. Intersection points are computed for

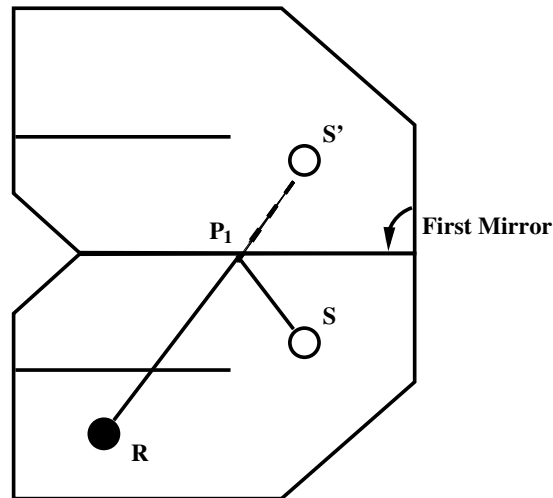


Fig. 3.5 An example of a path obstructed by a wall in a room. The path is invalid because the segment $\overline{RP_1}$ is truncated by the extruded wall.

every wall, then continuing with the in-path and in-polygon tests. If the point on the wall lies in the wall boundaries and in the sound path at the same time, the wall is found to obstruct the sound path, and the path should be deleted. If no wall is detected to intersect

with the segment, then the path is proved to be valid.

d. Back Tracing Test in High-Order Reflections

The validity tests above should go through every wall on each reflection, so they repeat many times in the inner loop. These tests only work on one segment of a path from one endpoint to another endpoint. As a result, in the N 'th reflection, there will be $N + 1$ series of test to perform and the computational burden will increase as the reflection order grows.

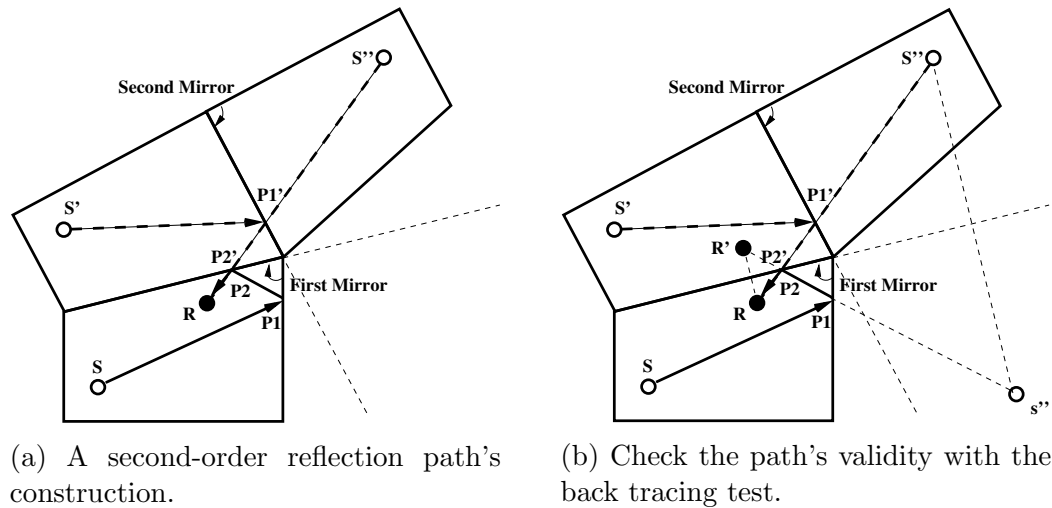


Fig. 3.6 Building the ray path with the Image Source Method (based on [8]). (a) Path $S-P_1-P_2-R$ is obtained by mirroring the source to the two surfaces marked in the picture. (b) The first collision point P_1 can be obtained by simultaneously mirroring the receiver and the second-order image source on the first mirror.

Figure 3.6 illustrates the examination procedure of a constructed path $S-P_1-P_2-R$. The sound source S is mirrored twice by two surfaces to the second-order image source S'' , as shown in Fig. 3.6(a). If the receiver R and S'' are linked together, the two image collision points can be obtained as P_1' and P_2' in the picture (P_2' is overlapped with P_2). We can get the positions of P_1 and P_2 by converting P_1' and P_2' to the original coordinates. In the practical path tests, however, the positions of reflection points are computed by converting the receiver and the image source to the corresponding coordinates as shown in Fig. 3.6(b). The validity test of the path is implemented as follows:

Step 1. Find the second intersection point P_2 by solving the equation Eq. (3.6) with the first reflection wall and the line linking the receiver and S'' .

Step 2. Once P_2 is found, the first section of the sound path $\overline{RP_2}$ is confirmed. The in-path test and the in-polygon test will be run on P_2 , and the visibility test will check if there exists any obstruction on $\overline{RP_2}$.

Step 3. If the first path section passes all the tests, the next section should be obtained by determining the position of the first collision point P_1 to continue the test. To obtain P_1 , the receiver R and S'' are mirrored by the first reflecting surface to R' and s'' , as shown in Fig. 3.6(b). Then P_1 is determined by solving the equation Eq. (3.6) with the line crossing R' and s'' and the second reflecting wall.

Step 4. The in-path test and the in-polygon test are applied to check the validity of P_1 . Then the visibility test will be added to the path $\overline{P_1P_2}$ and $\overline{SP_1}$.

Note that any failed step in the procedure above will lead to the elimination of that path. Fig. 3.6 only exhibits the 2D information in x and y coordinates. If coordinate z is taken into account, points in the picture will include different heights and collisions will occur on the ceiling and the floor.

3.1.4 Energy Calculation

The sound energy is represented as either sound power or sound intensity. It is typically easiest to compute these energies on a linear scale and then convert to decibels if needed [18]. As mentioned in the previous chapter, the sound energy is absorbed by the walls and the medium during the ray's propagation. The remaining power of the i th ray reaching the receiver can be expressed as [30]:

$$W_i = \frac{W_0 Q}{4\pi x^2} e^{-mx} \prod_{j=1}^J (1 - \alpha_j) \quad (3.7)$$

where W_0 is the power of the sound source, Q is the directivity pattern of the sound source, m denotes the air absorption coefficient, x represents the distance from the source to the receiver in this path, J is the number of reflections included in the path, and α_j is the corresponding wall coefficient on which the j 'th reflection has occurred.

3.2 Ray-tracing Approach

The implementation of the Ray-Tracing Method is similar to the Image Source Method in both the geometrical parts and the energy parts. Differences between the Ray-Tracing Method and the Image Source Method are reflected in two aspects. The first one is the ray initialization. As opposed to the source imaging process where ray directions are determined by the image sources positions, ray directions in the Ray-Tracing Method should be manually defined before running loops. The second difference is the way in which waves are assumed to impinge on a receiver. The receiver in the Ray-Tracing Method is regarded as a circular sphere instead of a point, with an assumed volume when calculating the energy. The following section will discuss these two unique aspects in the Ray-Tracing Method in detail.

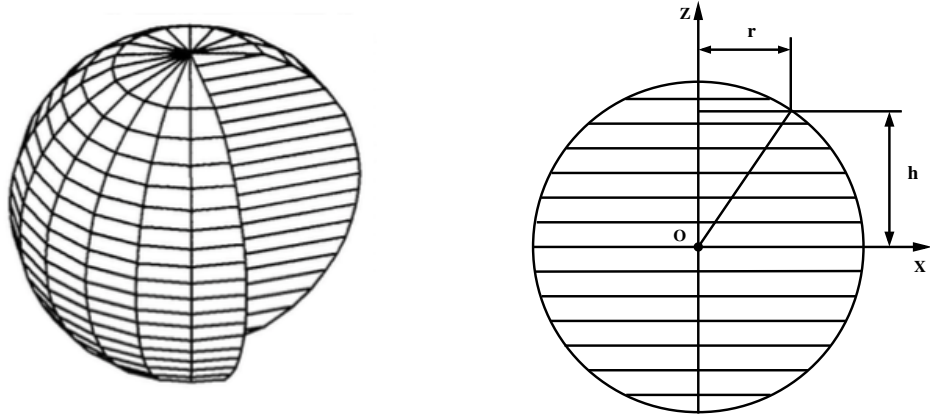
3.2.1 Ray Direction Initialization

The ray tracing method can be viewed as a stochastic process obeying the Monte Carlo theory. Instead of fully randomizing the propagation directions, some predefined conditions are added according to the characteristics of the sound source [44]. The sound source in the model is set as omnidirectional and it should emit sound rays uniformly on the surface of a unit sphere [44]. As a result, the unit sphere is cut into a large number of equal areas. Suppose that the total number of areas is N^2 . Then the sphere is divided into N sections vertically and N sections horizontally around the curvature, as shown in Fig. 3.7a. These areas are different in shape, but all of them are equal to each other in size. In order to obtain the vectors of the ray directions, we set the center of the sphere as the origin and the height of one layer h in the sphere, as shown in Fig. 3.7b, is expressed as:

$$h = \left| 1 - 2 \frac{i + rand1}{N} \right| \quad i = 0 \dots N - 1 \quad (3.8)$$

Here the first random number $rand1$ is in the range $[0, 1]$ and is introduced to cover the interval between two layers. After the determination of the height, the radius of the layer r in Fig. 3.7b can be calculated as:

$$r = \sqrt{1 - h^2} = 2 \sqrt{\frac{i + rand1}{N} - \left(\frac{i + rand1}{N} \right)^2} \quad i = 0 \dots N - 1 \quad (3.9)$$



(a) The unit source divided by N^2 areas (from [44])

(b) The profile of the unit circle

Fig. 3.7 Sound source is divided into uniform areas to generate ray directions.

To compute the ray direction on the xy plane, a second random number $rand2$ which is also in the range $[0, 1]$ is introduced to compute the exact angle:

$$\left(\cos \left(2\pi \frac{j + rand2}{N} \right), \sin \left(2\pi \frac{j + rand2}{N} \right) \right) \quad (3.10)$$

Thus the three components of the direction vector $\vec{n}_i(l, m, n)$ can be expressed as the following equation with only two random numbers:

$$l = 2\sqrt{\frac{i + rand1}{N} - \left(\frac{i + rand1}{N}\right)^2} \cos \left(2\pi \frac{j + rand2}{N} \right) \quad (3.11)$$

$$m = 2\sqrt{\frac{i + rand1}{N} - \left(\frac{i + rand1}{N}\right)^2} \sin \left(2\pi \frac{j + rand2}{N} \right) \quad (3.12)$$

$$n = 1 - 2\frac{i + rand1}{N} \quad (3.13)$$

$$i = 0 \dots N - 1, j = 0 \dots N - 1, rand1 \in [0, 1], rand2 \in [0, 1] \quad (3.14)$$

This method refines the method of simply generating random vectors with three stochastic numbers as the ray direction, which only produces directions on a surface of a cube, not

distributing a uniform spatial ray density.

3.2.2 Initial Ray Number Determination

Uncertainties are also introduced in the simulations by the use of a limited number of discrete rays to represent the sound [12]. To obtain impulse responses with good credibility, different parameters were introduced to obtain a quantitative measure of the Ray-Tracing Method error [36]. Due to the large ray number used in the calculation, the magnitude of result fluctuations is used as a credibility parameter. The magnitude of fluctuations is expressed as the mean of the absolute differences between two sound reverberant responses in two runs for the model. A reverberant response is calculated by the integration of a impulse response. In synthetic impulse responses, this procedure is equal to the sum of every peaks of it. For the Ray-Tracing Method, suppose a given impulse response is sampled into equally spaced histograms in time domain. The sum of the energy in one histogram of the impulse response ε_l can be represented as:

$$\varepsilon_l = \sum_{i=1}^{n_k} e_{i,k} \quad k = 1, 2, \dots, K \quad (3.15)$$

where n_k is the ray number in the interval, k is the interval index of a sampled impulse response, K denotes the total number of the intervals and $e_{i,k}$ is the energy of the i th ray ($i = 1, \dots, n_k$) in the k th histogram interval. Then successive value E_k is written in the following formula:

$$E_k = \sum_{l=k}^K \varepsilon_l \quad k = 1, 2, \dots, K \quad (3.16)$$

Figure 3.8 shows an energy response of a impulse response modeled by the Ray-Tracing Method. In early 0.1s with a sample rate of 48000Hz, the time interval is determined as 0.01s. Then the magnitude of fluctuations M in the given ray number can be calculated by summing the absolute subtractions of successive energy response:

$$M = \sum_{l=k}^K |E_l - E_{l+1}| \quad k = 1, 2, \dots, K \quad (3.17)$$

In this work, the magnitude of fluctuation M for a determined ray number in each room

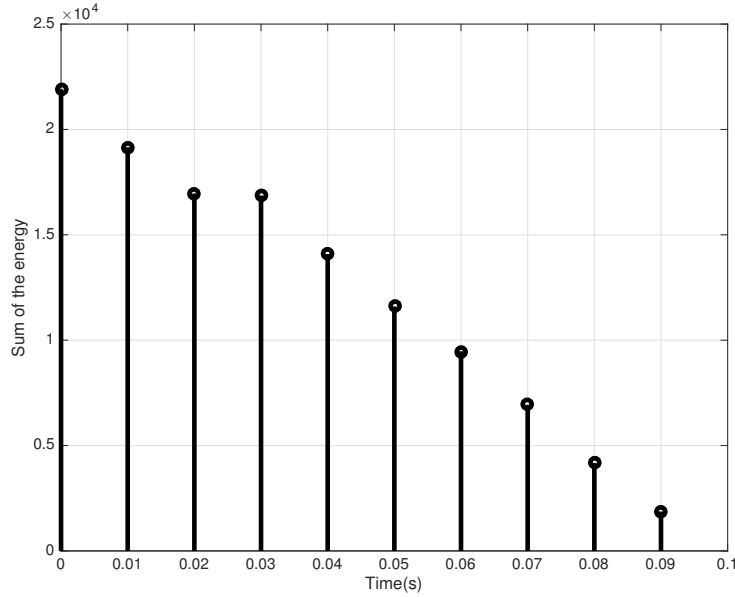


Fig. 3.8 Energy response of a impulse response implemented by the Ray-Tracing Method. The time of every interval is 0.01s, containing 480 samples in the sample rate of 48KHz.

is averaged over 20 runs. Figure 3.9 shows the simulation results of the magnitude of fluctuation versus ray number in four different rooms. All the curves converge to a constant value around 5×10^{-4} as the initial ray number increases. Considering both convergence and efficiency, the initial ray number of all room simulations was chosen to be $270 \times 270 = 72900$.

3.2.3 Sound Ray Reception

This section discusses how the receiver detects and records the arriving rays. The power W_i carried by the i th ray reaching the receiver can be expressed as Eq. (3.18):

$$W_i = \frac{W_0 Q}{N} e^{-mx} \prod_{j=1}^J (1 - \alpha_j) \quad (3.18)$$

where W_0 is the power of the sound source, Q represents the directivity coefficient of the sound source, N denotes the total ray number, m denotes the air absorption coefficient, L is

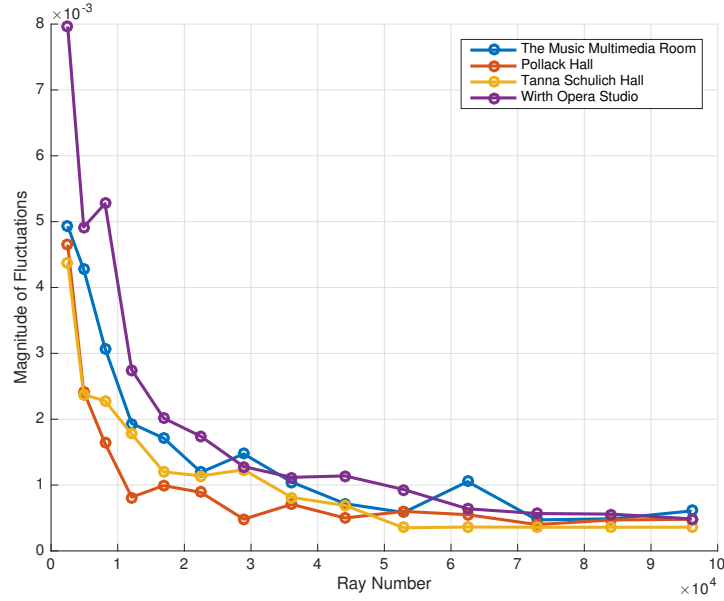


Fig. 3.9 Magnitude of fluctuations of four rooms measure in the experiments. Each curve takes an average of 20 runs.

the total distance the ray traveled from the source to the receiver, J denotes the reflection numbers in the path and α_j is the wall absorption coefficient of the wall in the j th reflection that the ray collides with.

If a ray has passed through the sphere of the receiver, the distance from the ray to the centre point of the receiver d must be smaller than the radius of the receiver r . So d can be expressed as the following formula:

$$d = \left[\frac{[(a - x_1)m - (b - y_1)l]^2 + [(b - y_1)n - (c - z_1)m]^2 + [(c - z_1)l - (a - x_1)n]^2}{l^2 + m^2 + n^2} \right]^{\frac{1}{2}} \quad (3.19)$$

where (a, b, c) are the coordinates of the sphere centre point, (l, m, n) is the vector of the line representing the ray path, (x_1, y_1, z_1) is a point on the ray path. Using the distance d we can obtain the distance the ray path travels in the receiver's sphere $d_{ri} = 2\sqrt{r^2 - d^2}$. Suppose the energy contributed by the i th path is written as:

$$E_i = W_i T_i \quad (3.20)$$

where T_i is the time spent by the wave reaching the receiver, which can be obtained from the total distance of the ray and the velocity. Finally, we can calculate the sound intensity of the ray impinging on the spherical receiver with a volume of V_r [39]:

$$I_i = \frac{E_i \cdot c}{V_r} = \frac{W_i \cdot T_i \cdot c}{V_r} = \frac{W_i \cdot d_{ri}}{V_r} \quad (3.21)$$

This value will be recorded in the time domain based on the time the ray spent during the propagation.

3.3 Echo Density

The echo density is a simple, robust measure to describe a reverberation impulse response [1]. The calculation is based on the fact that the impulse response peaks form a Gaussian distribution when the room is sufficiently mixed. Over a sliding window, the echo density profile $\eta(t)$ can be drawn as the fraction of the impulse response taps lying outside the window standard deviation:

$$\eta(t) = \frac{1}{\text{erfc}(1/\sqrt{2})} \sum_{\tau=t-\delta}^{t+\delta} w(\tau) \mathbf{1}\{|h(\tau)| > \sigma\} \quad (3.22)$$

where $h(\tau)$ is the impulse response, $\mathbf{1}\{\}$ is a bool function which returns 1 if the argument in it is true and zero otherwise, $\text{erfc}(1/\sqrt{2}) = 0.3173$ is the fraction of samples outside one standard deviation from the mean of a Gaussian distribution, $w(\tau)$ is the weighting function of the window and is normalized to have unit sum $\sum_{\tau} w(\tau) = 1$. δ is the value of half window size and σ is the window standard deviation:

$$\sigma = \left[\sum_{\tau=t-\delta}^{t+\delta} w(\tau) h^2(\tau) \right]^{\frac{1}{2}} \quad (3.23)$$

Figure 3.10 gives an example of echo density profiles with various window sizes from a measured room impulse response. The window function used in the computation is Hanning window. The general envelopes of the profiles are similar, with values ranging from

0 to around 1. Isolated early reflections tend to result in low echo density values due to their large standard deviation and a small number of samples outside the distribution. In contrast, dense reflections approximating Gaussian noise will have a high echo density near 1. For different window sizes, there are important differences in the profiles. Windows with short lengths have a relatively high variance about their local mean. As in Fig. 3.10, the variance of the curves decreases with increasing window length. In the late field, the mean values for larger window sizes are closer to 1, with less fluctuation. Too much variance will not make the profiles meaningful, thus a relatively large window size is required for computation. However, a window size that is too large will make the results less sensitive to local phenomena in the impulse responses. As a result, a window length of 20 ms is chosen as the appropriate window length for the analyses of this study.

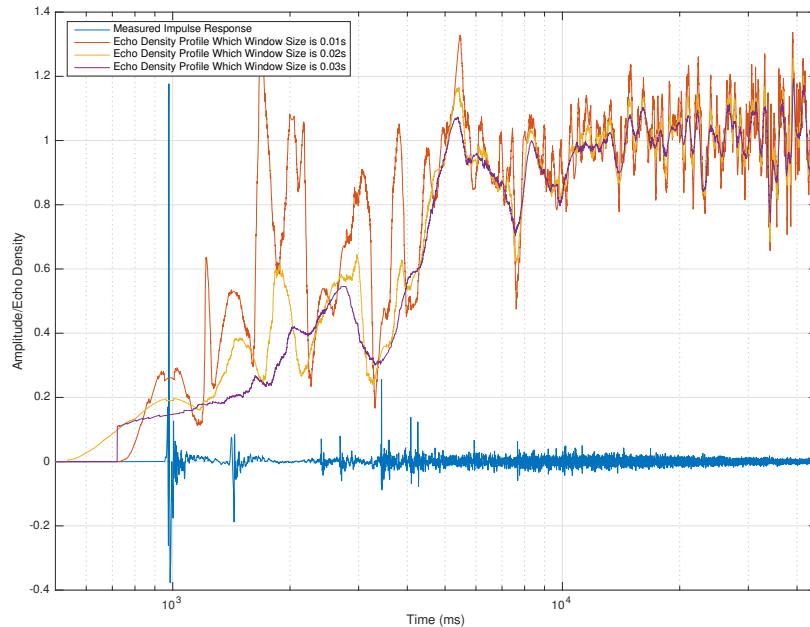


Fig. 3.10 Measured room impulse response (blue, 48 kHz samples) and its echo density profiles in different window sizes: 0.01(red), 0.02(yellow) and 0.03(purple)s. Note that the time axis is logarithmic.

Chapter 4

Measurements and Modeling Results

In this work, four real acoustic rooms are measured and modeled in the experiment. We mainly focus on the early parts of the impulse responses, therefore only the first 0.1s after the direct sound arriving at the receiver is compared with the computational results. A few studies specifically concerning early reflections have previously been reported. M. Barron and A. H. Marshall [45] have conducted a series of experiments with a simulation system to investigate the determinants of the subjective effect created by early lateral reflections, which were referred to as “spatial impressions.” J. S. Suha and P. A. Nelson [46] have compared the transient results of a phase image model with measurements in real rooms and demonstrated that the inclusion of complex reflections in the phase image model significantly increases the accuracy of the predictions. In that work, while impulse response shapes are thoroughly compared, specific early reflection timings were not analyzed in detail. Later, J. S. Bradley [47] presented results based on speech intelligibility tests in simulated sound fields and analyses of impulse response measurements in rooms used for speech communication. Lam investigated the problems of the diffuse-reflection coefficient that should be assigned to a wall in auditoria, and the prediction algorithm that may be used to model the diffuse reflections [22]. However, the work is less relevant to the goal of this thesis as it mainly focuses on the diffuse response rather than the early, specular response.

This chapter gives the details about the geometrical and acoustic descriptions of these enclosures and how their physical information is converted and stored as numerical data.

4.1 Room Measuring Methods

In the past, the measurement of impulse responses involved firing a pistol or popping a balloon in a room to produce a powerful impulse-like excitation. However, the use of loudspeakers emitting specialized signals is more common in modern experiments. This method provides a great variety of repeated signals, increases the signal-to-noise ratio and helps avoid some potential non-linear distortions, making it a better choice for most room impulse response measurements. Ideally, the sound source should be omnidirectional, emitting sound equally in all directions. If a speaker with directionality is applied in the measurement, directional distributions at different frequency bands must be modeled according to the speaker type. A single speaker is chosen in the room impulse response measurement as no omnidirectional speaker is available. In addition, because there is no official directional pattern published for the speaker in the experiment, a rough radiation distribution model is built and applied to all frequency bands to minimize the speaker's directional influence on the results, as shown in Fig. 4.1. The maximum energy is normalized at the front of

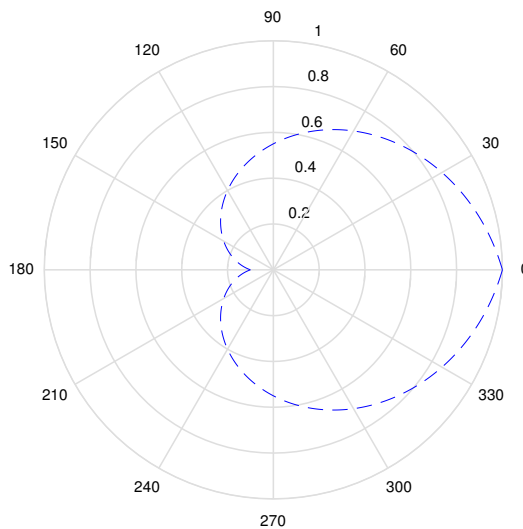


Fig. 4.1 Approximated directivity of the speaker in the model.

the speaker, which corresponds to an angle of zero degrees in a polar coordinate system.

The minimum energy, with a gain of 0.1, occurs at the rear of the speaker. The energy to the other directions is proportional to the angle between the emitting direction and the original direction θ :

$$E_{sp} = 1 - \frac{(1 - 0.1)\theta}{\pi} \quad (4.1)$$

Sound energy emitted from the speaker will be multiplied by E_{sp} according to the propagation directions, forming the radiation behavior of the speaker.

Similarly, omnidirectional microphones are most commonly used for receiving the sound in the rooms. An omnidirectional microphone was used in the experiment. In general, the microphone and the speaker are supposed to be as far from the walls as possible, while trying to avoid a symmetric configuration. We also used several different microphone positions to investigate the directionality of the speaker. The software used in the experiment and the following results and plots is Matlab R2015b and the interface used in the recording is RME Fireface 400. Table 4.1 shows all the items used for the room measurements. An omnidirectional microphone and a speaker are linked to a Fireface 400 interface connected to a Mac laptop. Matlab scripts, combined with C++ routines supporting realtime audio input and output, are used for sending and recording signals.

Table 4.1 Items used for room measurements

Name	Brand	Quantity
Computer	Mac Pro	1
Software	Matlab	1
Microphone	Sencore SP-PMIC1	1
Speaker	Meyer UPJ-1P	1
Interface	RME Fireface 400	1

There are many ways of taking room measurements. Muller and Massarani [48] and Stan et al. [49] published their studies comparing various measuring methods for room impulse responses. According to their studies, sine sweeps have more advantages in obtaining high signal-to-noise ratios and eliminating most distortion. In this work, we use log sine sweep signals, signals with exponentially increased frequency, as the exciting signal to obtain the room impulse responses [50]. The expression of the signal can be written as:

$$s(t) = \sin \left(\frac{2\pi f_1 T}{\ln \frac{f_2}{f_1}} \left(\exp\left(\frac{\ln(\frac{f_2}{f_1})t}{T}\right) - 1 \right) \right) \quad (4.2)$$

where f_1 is the starting frequency set as $20Hz$, f_2 is the ending frequency set as $20000Hz$ and T is the total duration. The spectrum of the signal is proportional to $1/f$, corresponding to 3 dB per octave. The duration T must be long enough to reduce the growth rate of the frequency, for there is some ripple at the areas of two truncated frequencies and a lower slope can minimize such influence. The encoded impulse response can be retrieved by an acyclic frequency-domain deconvolution technique. This involves zero-padding the source signal $s(t)$ and measured response $y(t)$ in the time domain, dividing them in the frequency domain, and transforming the result back to the time domain:

$$h(t) = IFFT_k \left(\frac{Y(\omega_k)}{S(\omega_k)} \right) \quad (4.3)$$

where $Y(\omega_k)$ and $S(\omega_k)$ are FFTs of $y(t)$ and $s(t)$.

4.2 Room Details and Results

In this section, the modelling and experimental results for the four rooms considered in this study are described. All the results including the 3D model plots, the IR curves and the echo densities are computed with Matlab. Sound levels of measured impulse responses and simulated ones are normalized by their maximum power for clear comparison. The selected rooms include the Music Multimedia Room (MMR), Pollack Hall, Tanna Schulich Hall and the Wirth Opera Studio. The following part will introduce these rooms and their models in order. Physical coefficients used in all these models are listed in Table 4.2.

Table 4.2 Physical Coefficients in Room Models

Name (Unit)	Value
Total Time (s)	0.1
Sound Velocity (m/s)	343.82
Frequency Band (Hz)	1000
Temperature ($^{\circ}C$)	20.7
Air Absorption Coefficient	0.003

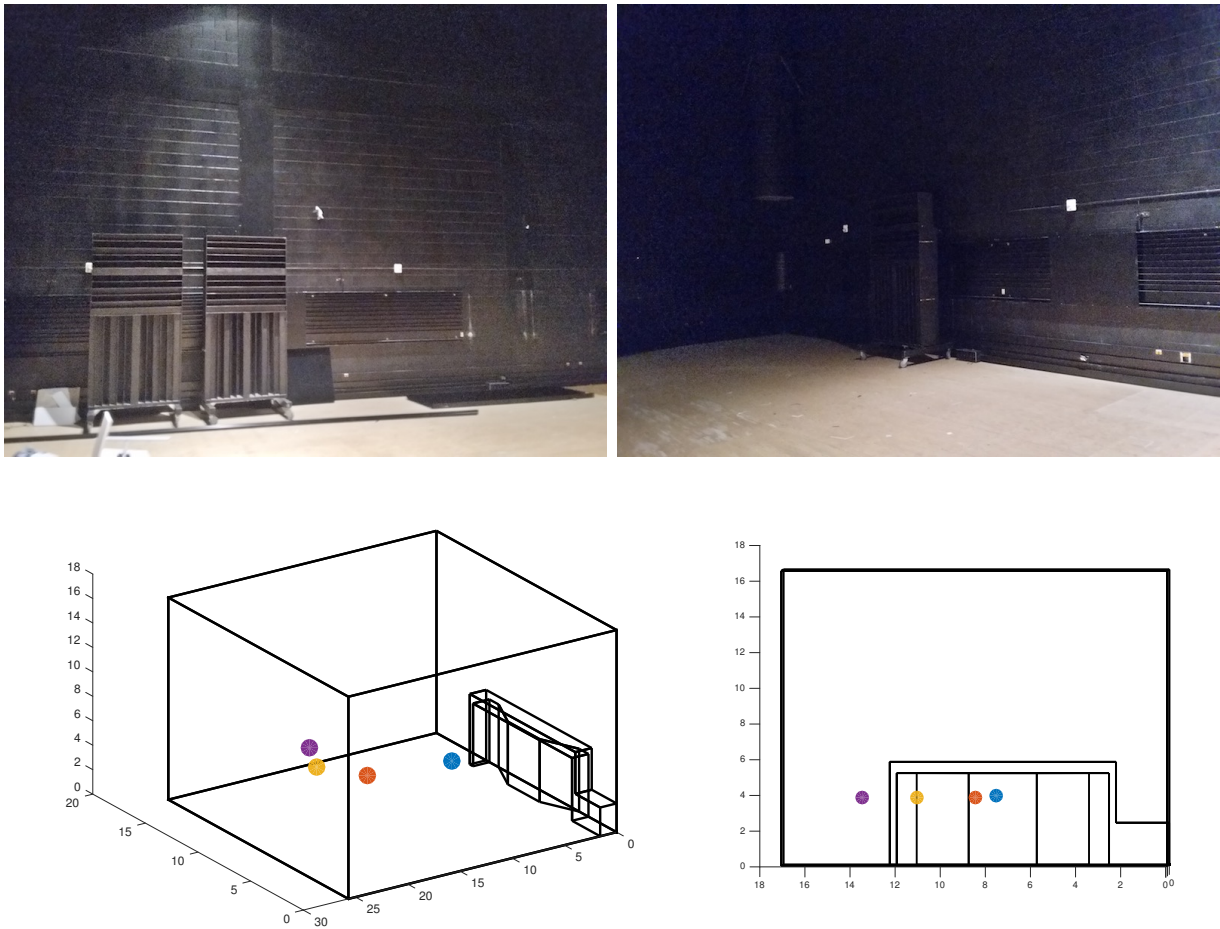


Fig. 4.2 Views of Music Multimedia Room and its 3D model. The blue point represents the position of the speaker S_1 , the red point represents the first position of the microphone R_1 , the yellow point represents the second position of the microphone R_2 , the purple point denotes the third position of the microphone R_3 . All the points' coordinates are listed in Table 4.4.

4.2.1 The Music Multimedia Room (MMR)

The Music Multimedia Room is the enclosure that is most like a rectangular box among all the measured rooms. The dimensions of the room are $17.1m \times 25.7m \times 16.5m$ with a volume of around $7263m^3$. The room mainly consists of four materials. The absorption coefficients of each material on each frequency band are listed in Table 4.3. Most data are determined according to the database developed by Ingolf Bork in the project of the Round Robin

on room acoustical computer simulations [51–53]. Other data were obtained from product data given by manufacturers [7]. The bounding walls are made of cinderblock, with the floor made of plywood and the ceiling made of steel frames. Figure 4.2 gives some photos and some views of the room model. The control room space in the south of the room has been built in the model. The periphery of the control room is covered with plaster and with some metal handrails attached above it, but the handrails are not included in the digital model. Also, there are steel stairs in the right corner which are not included in the model. Additionally, the black panels on the side walls and the details near the ceiling (ventilation ducts, suspended walkway,) are not included. Measurements are taken three times with one fixed speaker placed in the south and a microphone in three different positions in the north. The coordinates of the speaker and the microphone speakers are listed in Table 4.4.

Table 4.3 Material absorption coefficients in the Multimedia Room

Frequency Band	125	250	500	1000	2000	4000
Side walls (cinderblock)	0.02	0.02	0.03	0.03	0.04	0.05
Side walls (plaster)	0.02	0.02	0.03	0.03	0.04	0.05
Floor (wood)	0.42	0.21	0.1	0.08	0.06	0.06
Ceiling (steel frame)	0.15	0.1	0.06	0.04	0.04	0.05

Table 4.4 Location of source S_1 and receivers R_1, R_2, R_3 in the Multimedia Room (m)

Points	S_1	R_1	R_2	R_3
X	7.64	8.53	13.57	8.82
Y	8.05	15.25	15.75	16.65
Z	3.89	3.79	3.79	3.79

The differences between the measured impulse response and the modeled impulse response are compared with each other in different octave bands filtered by each band’s central frequency for the MMR. Figure 4.3 presents the simulation results of the Image Source Method in six different octave bands. The energy varies in each octave band and the impulse responses have slightly different shapes, with more smoothing at lower frequency bands. Therefore, timing estimations are more precise in the high-frequency bands.

Thus, the 1000Hz frequency band is selected as the primary frequency range for most of the following analysis and discussion. The air absorption coefficient will also be 0.0013 according to Table 2.2 in Chapter 2.

To check the simulation accuracy, impulse responses from the two models and the measurement are combined for comparison. Figure 4.4 shows the measured and modeled impulse responses filtered by a second-order Chebyshev bandpass filter from the Image Source Method and the Ray-Tracing Method in the 1kHz octave band. The speaker is placed at S_1 and the microphone is placed at R_1 , the coordinates of which are shown in Table 4.4. Only the first two reflection orders are implemented in the two models and the model results are normalized by the maximum peak (which is the direct sound energy) of the measurement response. The results of both the Image Source Method and the Ray-Tracing Method are well fit in time and energy and are consistent with the measured impulse response, with peaks at around 0.03s, 0.052s, and 0.058s. After 0.06s deviations between the measurement result and the model results become larger. There are two peaks in the model at 0.0594s and 0.0635s that are not evident in the measurement result in Fig. 4.5. From the 3D geometric model, we can see the first ray path, which is a first-order reflection, is emitted from the speaker (represented by the blue node in the photo) and bounces off the wall behind the speaker to finally reach the receiver (represented by the red node). The second ray path first bounces off the back wall as in the first path, then collides with the floor to finally reach the receiver. Both paths are emitted from the back of the speaker and should be attenuated according to the radiation distribution function. As the peaks are not apparent in the measured results, it is assumed that the energy emitted from the back of the speaker is too small to generate significant peaks when arriving at the receiver. As a result, the differences may come from the directionality model of the speaker and a more accurate model should be implemented to reduce the deviation. Another apparent difference between the measurement and the modelled results is the peak at around 0.073s. As the peak does not appear in both Image Source Method and Ray-Tracing Method, we assume it is from other room structures, such as the ducts near the ceiling that are not included in the geometric model.

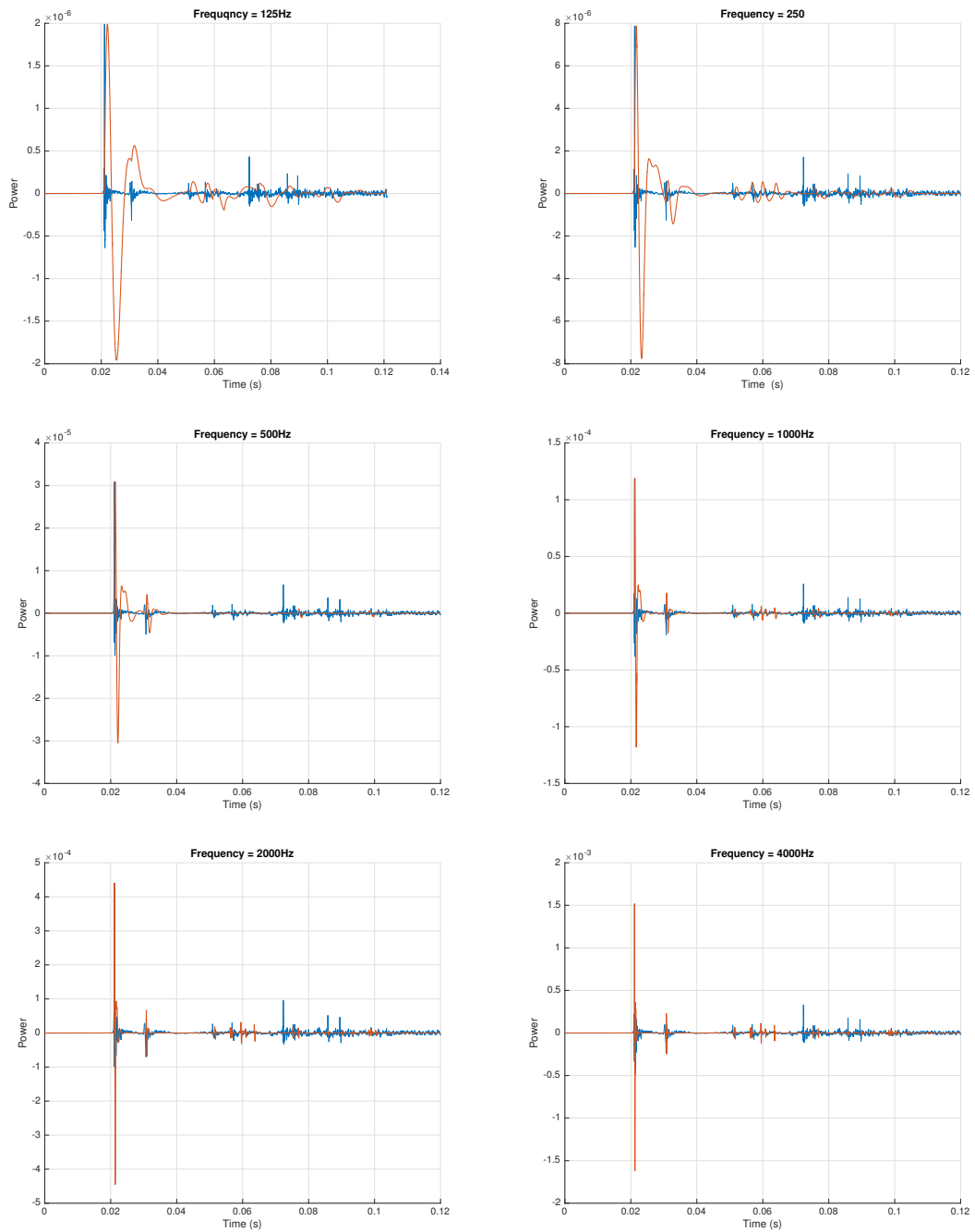


Fig. 4.3 Comparison between measured impulse responses and modelled impulse responses with the Image Source Method in different octave bands. The source and the receivers' positions are at S_1 and R_1 .

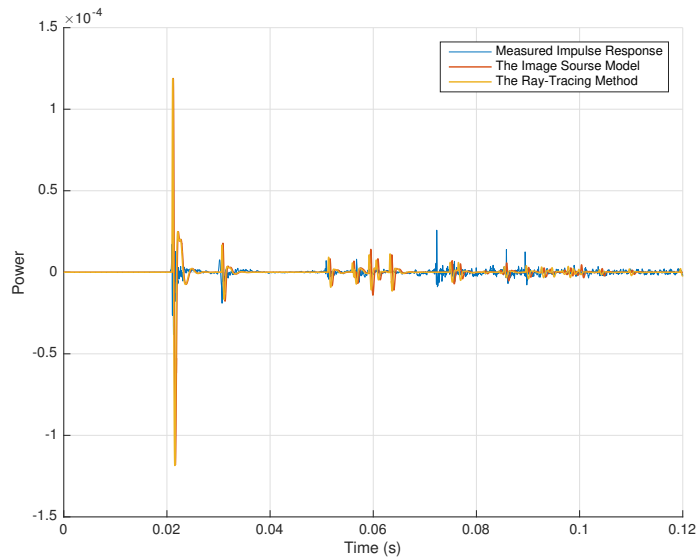


Fig. 4.4 Impulse responses of the measurement and modeled results at the 1kHz octave band in the Music Multimedia Room. The blue curve represents the measurement result, the red curve represents the simulated IR from the Image Source Method, and the yellow curve is the result from the Ray-Tracing Method.

To further investigate the sound reflection behaviours in the room, we can compute the echo density profiles for both the modelled and experimental results [1]. Figure 4.6a presents the echo densities of the previous three impulse responses. The window used in the profiles is hanning window and length is 0.02s. The curves from the Image Source Method and the Ray-Tracing Method are consistent in the graph. They both have three main crests and fall at around 0.04s and 0.1s. The differences between the simulation result and the measurement result come from the geometrical structure discrepancies between the 3D model and the real room structure. The biggest difference between the measurement result and the modelled result is in the range between 0.04-0.05s, where the local peak in the measurement is not found in the model results. However, there is no evident peak among the three impulse responses. There are two assumptions for the difference. The first one is that there exist noise peaks in this interval that increase the density of the modes. The second one is that the high peak is the density of the diffuse sound from the first reflection at around 0.03s. The following section will conclude the reason of the difference.

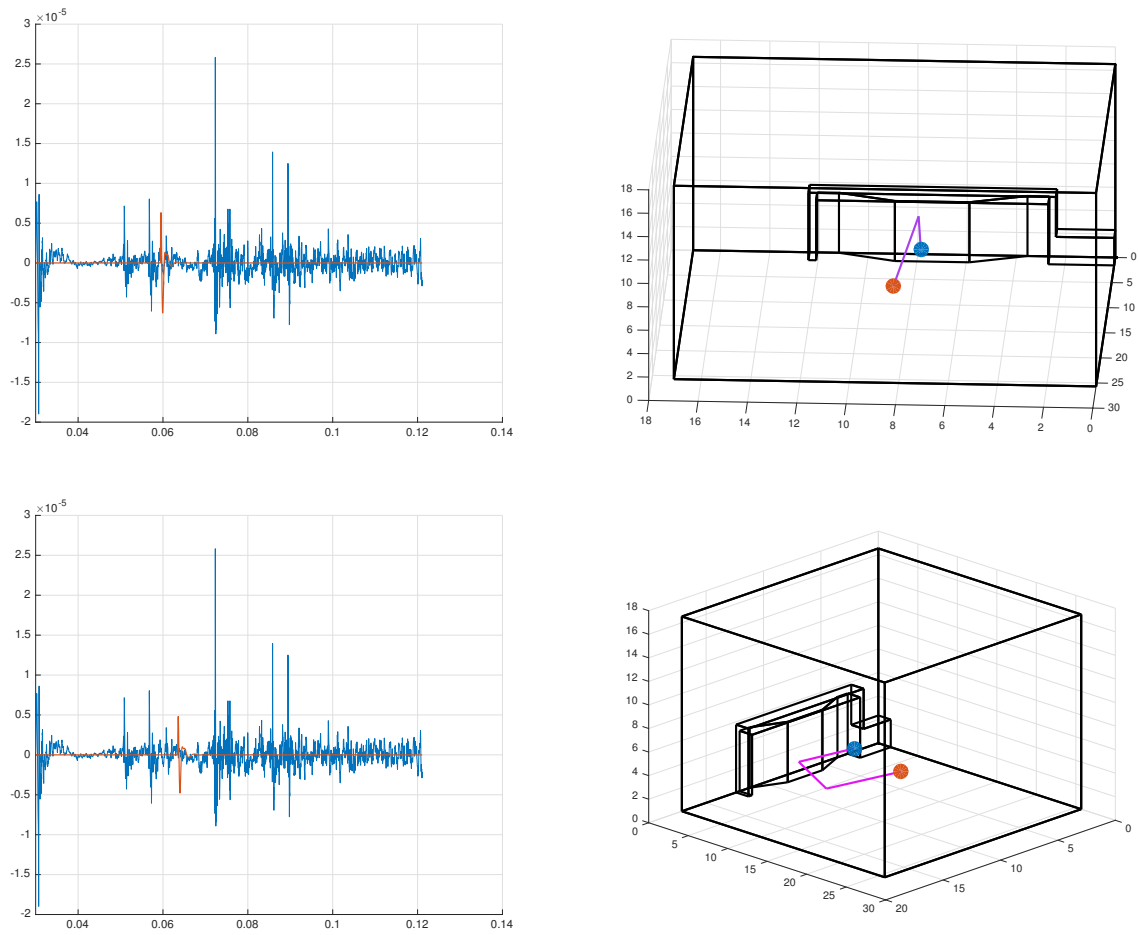


Fig. 4.5 Two peaks appearing in the model results are not found in the experimental results for the MMR. The blue dot in the right figures represents the speaker placed at S_1 and the red dot denotes the microphone placed at R_1 as in Table 4.3.

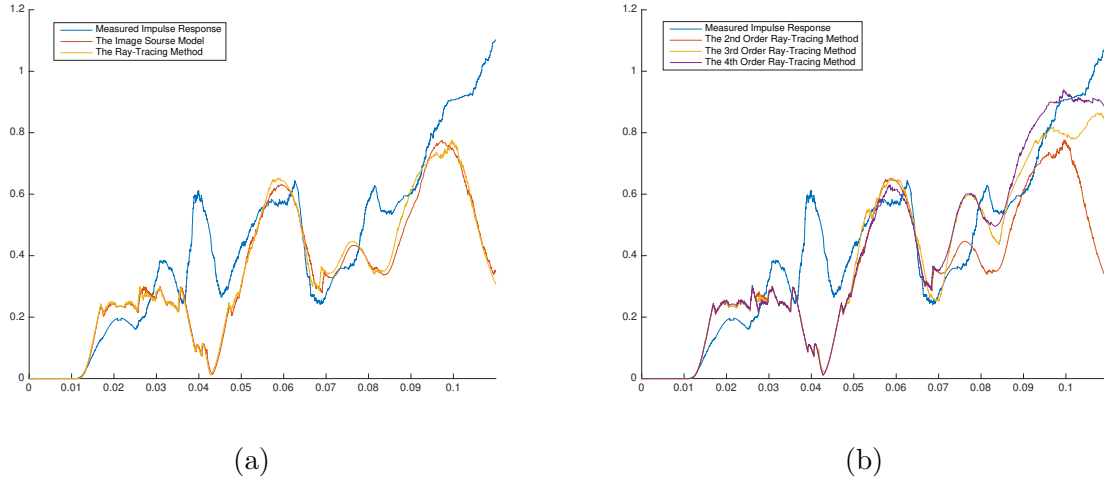


Fig. 4.6 (a) Echo densities [1] of the measurement and modelled results in Fig. 4.4. The blue curve represents the measurement result, the red curve represents the simulation IR from the Image Source Method, and the yellow curve is the result from the Ray-Tracing Method. (b) Echo densities of the measurement impulse response and the modelled results by the Ray-Tracing Method with different reflection orders: second-order echo density profile (red), third-order echo density profile (yellow) and fourth order echo density profile (purple).

The modelled results and the measurement result display different trends after 0.07s. To investigate the variation of the curves after 0.07s, echo density profiles with the Ray-Tracing Method in different reflection orders were built as shown in Fig. 4.6b. As the order increases from second to fourth, the tails of the echo density curves start to get closer to one. We can conclude that the drop of the echo density curves for the first two reflection orders after 0.09s is caused by the lack of later, higher-order reflections. The rise of the echo density after 0.007s is partly caused by the involvement of the late orders of the reflection modes. Another factor increasing the echo density values in the measurements is the likely presence of diffuse (non-specular) reflections, which increase the echo density in the region following a reflection.

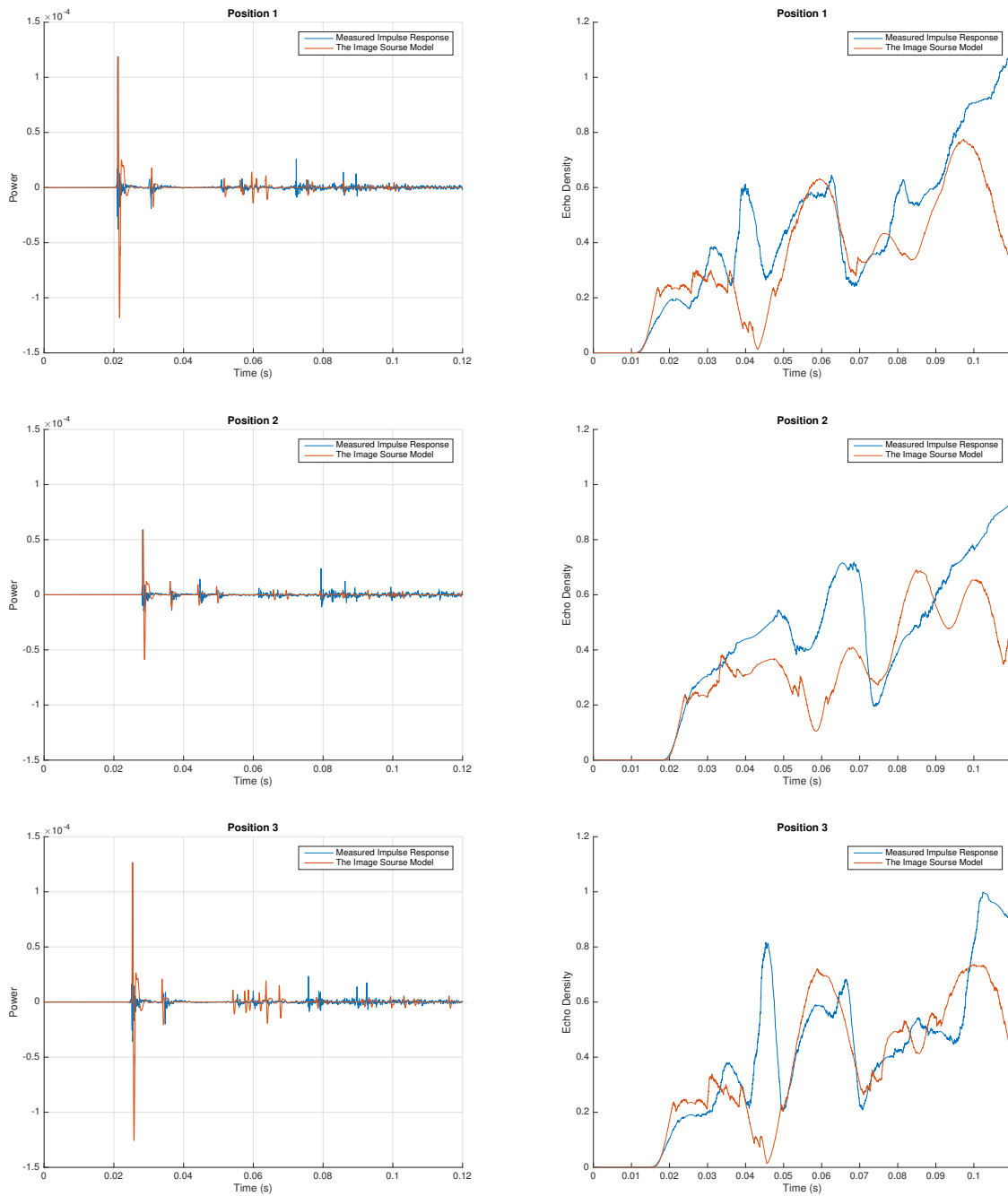


Fig. 4.7 Impulse responses and echo densities in three different receiver positions.

The peak positions in each modeled impulse response depend on the source and the

receiver positions. Figure 4.7 shows the impulse responses and echo densities at three positions between the measurement response and the Image Source Method's impulse response. The center frequency of the octave band is 1000Hz. From the three echo density comparison graphs, it can be seen that the modeled echo density curves are relatively close to those of the measurements in all three figures. This means MMR has relatively high specular properties. In other words, there is generally less non-specular scattering of waves from the various room surfaces. This is caused by the low diffuse effects of the side walls made up of cinder blocks, where most energy components in reflections from the walls are easily identified as spikes in the impulse responses. Another phenomenon that should be noticed is that the crest of the measurement responses between 0.04s and 0.06s, as in the first graph of Fig. 4.6a, shifts to the interval between 0.06s and 0.07s in the second graph due to the change in the receiver's position. The energy of the crest is much higher than the crest in the modeled result, indicating there exists additional energy in the crest apart from the specular reflections. Therefore, there are more reasons to believe that the diffuse reflection causes the crest after the first reflection.

4.2.2 Pollack Hall

Pollack Hall is a concert hall in the Strathcona Music Building of McGill University. It is the largest performance venue in the Schulich School of Music with 600 seats [54]. Some photos of the real room and the model are shown in Fig. 4.8. The top view of the hall looks like a bell with two side walls angled at the stage. The floor of the auditorium is made up of rising steps and the entrance is in the middle of the steps. The dimensions of the hall are $18m \times 36m \times 12.65m$ with a volume around $6952.5m^3$. The side walls of the hall are mainly plaster, the stage is made up of wood, and stairs in the audience area consist of carpet and gypsum board. The back wall is covered by wood with irregular shapes, which is simplified by a plane with special absorption properties. Relevant information about the materials is listed in Table 4.5.

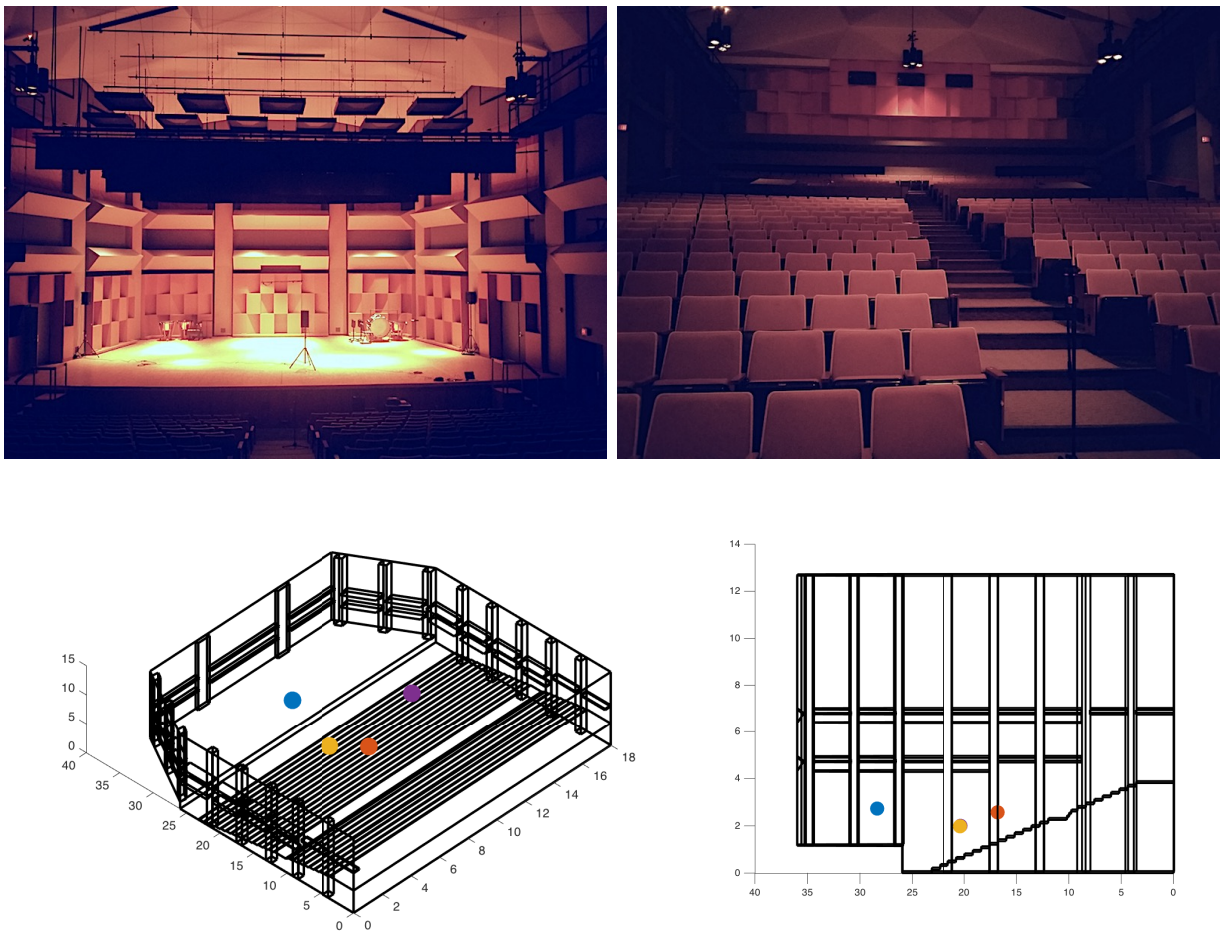


Fig. 4.8 Views of Pollack Hall and its 3D model. The blue point represents the position of the speaker S_1 , the red point represents the first position of the microphone R_1 , the yellow point represents the second position of the microphone R_2 , the purple point denotes the third position of the microphone R_3 . All the points' coordinates are listed in Table 4.6.

Besides the general shape of the hall, the model includes details of the stage, stairs of the auditorium, and the vertical and horizontal columns on the wall. The polygons on the ceiling and the chairs are not modelled, nor are the panels on the roof. There are three measuring positions. The speaker is at the center of the stage without further movement with one microphone placed in three positions at the audience seats. Table 4.6 shows the exact coordinates of each measuring point.

Table 4.5 Material absorption coefficients in the Pollack Hall

Frequency Band	125	250	500	1000	2000	4000
Back Wall (absorption wood)	0.05	0.05	0.2	0.3	0.4	0.45
Side Wall (acoustical plaster)	0.17	0.36	0.66	0.65	0.62	0.68
Floor (carpet)	0.1	0.4	0.62	0.7	0.63	0.88
Stage (wood)	0.1	0.07	0.06	0.06	0.06	0.06
Ceiling (steel frame)	0.15	0.1	0.06	0.04	0.04	0.05
Columns (plaster)	0.02	0.02	0.03	0.03	0.04	0.05
Stairs (gypsum board)	0.3	0.69	1	0.81	0.66	0.62

Table 4.6 Location of source S_1 and receivers R_1 , R_2 , R_3 in the Pollack Hall (m)

Points	S_1	R_1	R_2	R_3
X	9	9	7.93	13.67
Y	28.38	16.83	20.42	20.39
Z	2.68	2.54	1.94	1.93

Comparisons between the measured impulse response and the modeled impulse responses are shown in Fig. 4.9a. The source is at the position of S_1 and the receiver's position is at R_1 as in Table 4.6. It is hard to distinguish large specular peaks in the measurement result, indicating that the walls in Pollack Hall have a large diffuse effect. Because of the large volume of the hall among the enclosures, it takes more time for the sound to propagate from the stage to the audience. Thus the time of the direct sound is the longest (given our receiver positions) in Pollack Hall. As for the modeled impulse responses, the main reflections are at around 0.063s, 0.067s and 0.078s in both the Image Source Method and the Ray-Tracing Method. These reflections are all from the first-order reflections. Although the overestimation could be due to the underestimation of the absorption coefficients of the materials of the walls, There is a great probability that most of the energy in those evident

spikes is scattered in the collisions during the sound propagation. There are additional reflections in the Ray-Tracing Method in the first 0.06s. This is because the receiver has an assumed volume that causes rays passing near the R1 position to be included in the result. In reality, these paths are formed by other obstacles like chairs that are not included in the model.

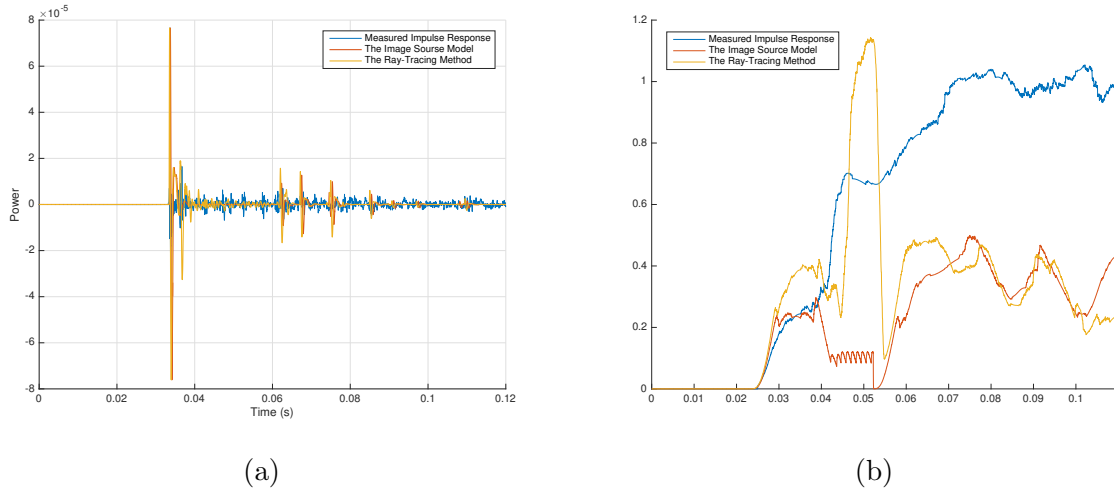


Fig. 4.9 Impulse responses and echo density curves of the measurement and modeled results at 1kHz octave band in Pollack Hall. The blue curve represents the measurement result, the red curve represents the simulation IR from the Image Source Method, and the yellow curve is the result from the Ray-Tracing Method.

Figure 4.9b reflects the echo density distribution of the three impulse responses. From the echo density curve of the measured impulse response, the echo density rapidly rises to 1 at 0.07s, which is faster than that in the MMR. Meanwhile, the echo density curve of the Image Source Method never passes 0.6 in the first 0.1s. The majority of the echo density curve in the Ray-Tracing Method does not pass 0.6s except the segment between 0.04s and 0.06s where the density seems overestimated. Note that the Ray-Tracing impulse response has a larger echo density than the other impulse responses from the direct sound time to 0.06s, while the echo density curve from the Image Source Method has the lowest value in this period. After 0.06s, the two modelled curves have similar trends. Therefore, some details of the digital model should be revised to reduce the variations in the first 0.06s. The difference between the value of the measured echo density curve and the modelled echo

density curve is much larger than the difference in the MMR after 0.06s, illustrating that there is more diffuse scattering at the surfaces in Pollack Hall.

4.2.3 Tanna Schulich Hall

Tanna Schulich Hall, opened in 2006, is a multipurpose venue located in McGill’s Wirth Music Building (formerly called the New Music Building) with 187 seats [55]. It is commonly used as a concert, lecture and conference room. The general shape of the hall is similar to Pollack Hall, but the size is much smaller than that of Pollack Hall. The dimensions of the hall are $12m \times 14.4m \times 7.11m$ with a volume of approximately $1312m^3$. The upper side walls are covered with a comb-like wooden structure, and the lower parts are covered with gypsum. The stairs in the auditorium are also made up of gypsum, and the ceiling consists of plaster panels each with different angles. The stage is also made of wood. Absorption coefficients of each material in different octave bands are listed in Table 4.7

The computer model of Tanna Schulich Hall includes the stage, the stairs of the auditorium and the handrails on both sides of the hall. The complex shape of the ceiling is represented by a plane with special absorption properties, and the physical shapes of the chairs are not included in the model. During the measurement, the speaker is placed in the center of the stage pointing to the auditorium. The microphone is placed in three different positions in the auditorium. Table 4.8 presents the details of each position in the measurement.

Table 4.7 Material absorption coefficients in the Tanna Schulich Hall

Frequency Band	125	250	500	1000	2000	4000
Side Walls and Stairs (gypsum)	0.30	0.69	1	0.81	0.66	0.62
Stage (wood)	0.1	0.07	0.06	0.06	0.06	0.06
Stair Handrail (steel frame)	0.15	0.1	0.06	0.04	0.04	0.05
Ceiling (acoustical plaster)	0.17	0.36	0.66	0.65	0.62	0.68
Side Walls (RPG QRD)	0.06	0.15	0.45	0.95	0.88	0.91

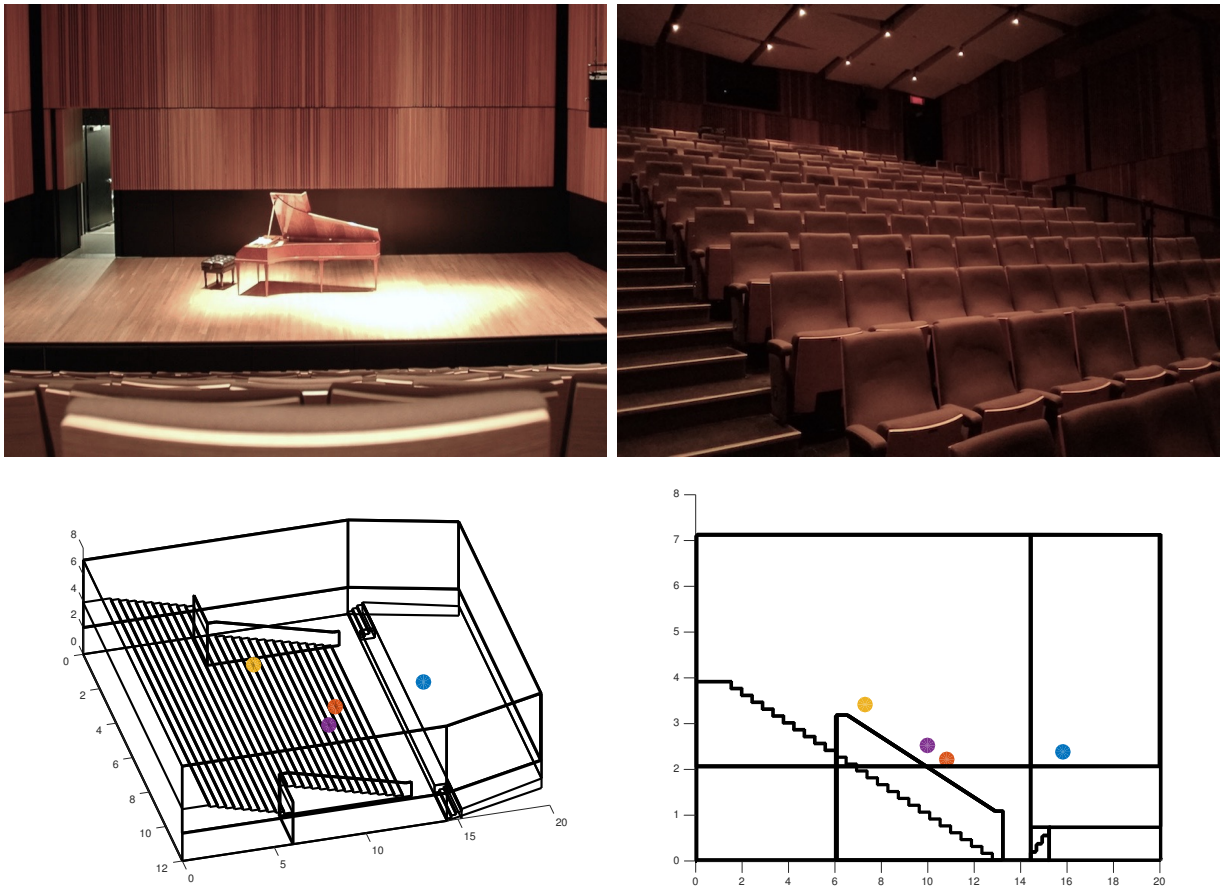


Fig. 4.10 Views of Tanna Schulich Hall and its 3D model. The blue point represents the position of the speaker S_1 , the red point represents the first position of the microphone R_1 , the yellow point represents the second position of the microphone R_2 , the purple point denotes the third position of the microphone R_3 . All the points' coordinates are listed in Table 4.8.

Table 4.8 Location of source S_1 and receivers R_1 , R_2 , R_3 in the Tanna Schulich Hall (m)

Points	S_1	R_1	R_2	R_3
X	6	6.51	4.4	7.65
Y	15.8	10.79	7.27	9.92
Z	2.37	2.21	3.41	2.51

As the microphone is placed close to the speaker in a smaller room among the other enclosures, the direct sound quickly reaches the receiver in Tanna Schulich Hall. Figure 4.11a shows the impulse responses obtained from the models and measurements. The following reflection peaks then get denser, and the distinguishable reflections appear earlier than in previous cases, which is consistent with the modelled results. However, the large peaks in the modeled results are still larger than the corresponding peaks in the measured curve that are not significant in the impulse response, indicating that much energy in the sound waves has been absorbed or diffused during the propagation. Considering that the walls in Tanna Schulich Hall contain many irregular shapes, as seen in Fig. 4.10, the diffusion likely contributes more to the energy loss.

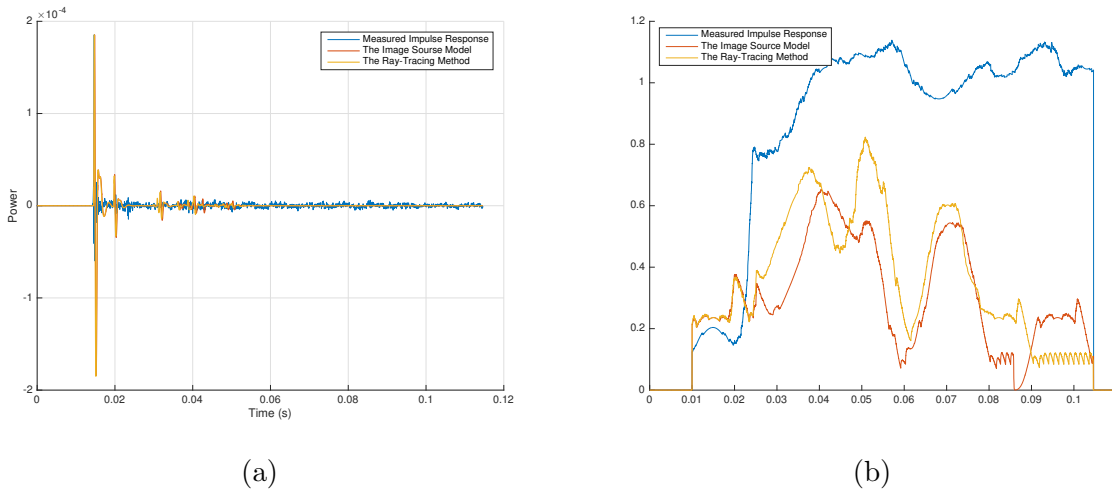


Fig. 4.11 Impulse responses and echo density curves of the measurement and modelled results at 1kHz octave band in the Tanna Schulich Hall. The blue curve represents the measurement result, the red curve represents the simulation IR from the Image Source Method, and the yellow curve is the result from the Ray-Tracing Method.

From Fig. 4.11b, it can be noted that the hall quickly generates its echo density in the first 0.04s. This time is much faster than that in the Pollack Hall. This phenomenon demonstrates that sounds in the Tanna Schulich Hall will experience more diffuse scattering effects when they interact with the walls. Another indicator of the fast diffusion is the jump at between 0.02s and 0.025s in the measured curves. The modelled curves between 0.02s and 0.025, which only contain the specular reflections, increase slowly, so there must be a lot

of irregular scattering generated in this period. Massive diffusion and high order reflections maintain the echo density value at around one even though the specular components start to decline after 0.05s as in the model results.

4.2.4 The Wirth Opera Studio

The Wirth Opera Studio is located in McGill’s Elizabeth Wirth Music Building. It is used for opera rehearsals, recording sessions and research projects [56]. It is an approximate cuboid room, but there are other obstacles displayed in the room during the measurement as shown in Fig. 4.12. There are some curtains covering parts of the side walls, some stage props at the corner, a piano and some tables lying in the room and some chairs on the steps arranged in a row to the south of the room. We denote the material of the side walls as plaster and assume the floor to be wood. The chairs are assumed to be made of a material with special coefficients in each octave band. Details of the material properties are shown in Table 4.9. The dimensions of the room are $12.42m \times 20.18m \times 5.99m$ with an approximate volume of $1396m^3$.

The model of the room includes the prominent upper walls, a rectangular column in the room and a piece of curtain hanging on the right side of the room. The chairs are represented by some thin panels in the south. The speaker is placed near the column side and points to the chairs. The microphone is positioned in three different positions near the chairs. Coordinates of the source and microphone’s positions are listed in Table 4.10.

Table 4.9 Material absorption coefficients in the Wirth Opera Studio

Frequency Band	125	250	500	1000	2000	4000
Side walls (gypsum)	0.30	0.69	1	0.81	0.66	0.62
Curtain	0.36	0.26	0.51	0.45	0.62	0.76
Side walls (plaster)	0.02	0.02	0.03	0.03	0.04	0.05
Floor (wood)	0.1	0.07	0.06	0.06	0.06	0.06
Chairs	0.40	0.50	0.58	0.61	0.58	0.5

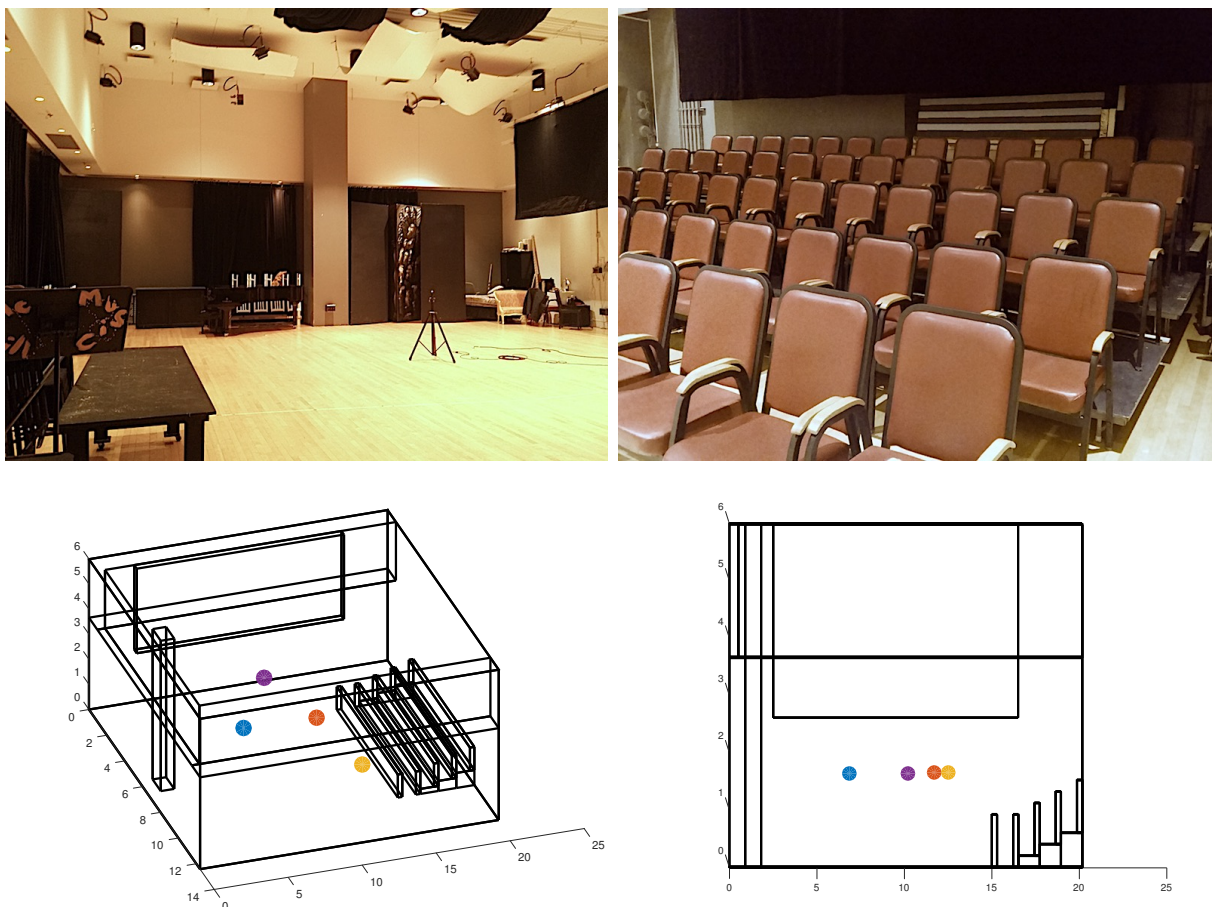


Fig. 4.12 Views of the Wirth Opera Studio model. The blue point represents the position of the speaker S_1 , the red point represents the first position of the microphone R_1 , the yellow point represents the second position of the microphone R_2 , the purple point denotes the third position of the microphone R_3 . All the point's coordinates are listed in Table 4.10.

Table 4.10 Location of source S_1 and receivers R_1, R_2, R_3 in the Wirth Opera Studio (m)

Points	S_1	R_1	R_2	R_3
X	5.98	6.09	9.89	2.73
Y	6.86	11.73	12.52	10.21
Z	1.64	1.65	1.65	1.65

The Wirth Opera Studio is also a small room, but the specular components in the early period are more obvious than those in the Tanna Schulich Hall, as shown in Fig. 4.13a. The specular reflections still have little energy compared to the modelled results. The modeled impulse responses have more energy in the first 0.05s than that of the measurement. The main reflections in the two modeled impulse responses are consistent with each other, but some reflections such as the one at around 0.03s do not match the ones in the measured response. This could be due to the lack of details of the model that only consists of simple structures in the path of distinguishing peaks.

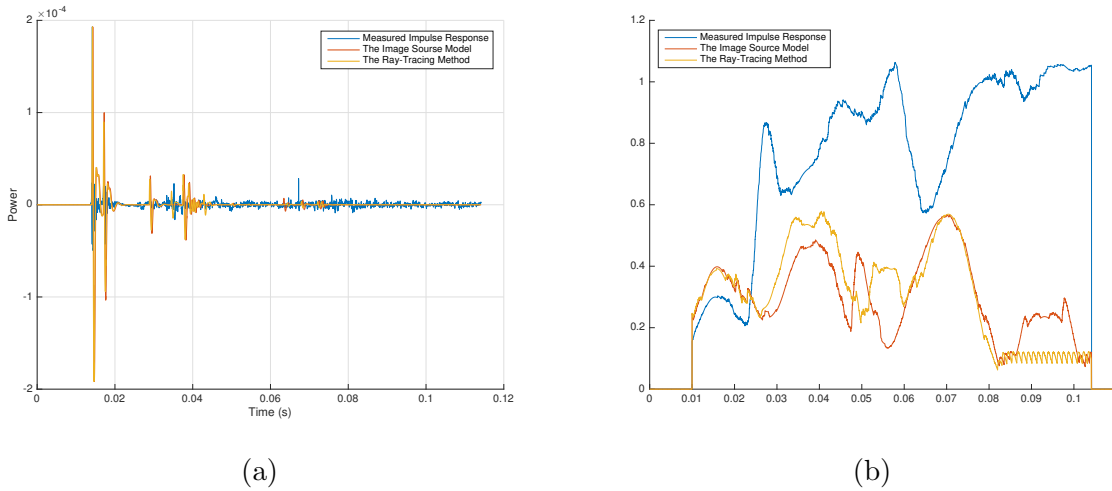


Fig. 4.13 Impulse responses and echo density curves of the measurement and modelled results at 1kHz octave band in the Wirth Opera Building. The blue curve represents the measurement result, the red curve represents the simulation IR from the Image Source Method, and the yellow curve is the result from the Ray-Tracing Method.

From Fig. 4.13b we can see the sounds in the studio are rapidly diffused as the echo density quickly rises after 0.02s. The density of the specular reflections has a crest between 0.03s and 0.04s. Meanwhile, the measured density increases steady toward 1 after the earliest reflections but then drops to 0.6 around 0.05s. The great ups and downs in the measurement curve suggest that the sound field in the studio is not entirely diffuse as in the two concert halls. The next growth of the echo density in the measured curve is after the second specular crest between 0.06s and 0.08s. Then the specular components of the first two reflection orders begin to decrease, but the diffusion and high order reflection modes

hold the total echo density around 1.

4.3 Summary of Results

Different parameters in geometric acoustic models play different roles in simulating the early reflections. The accuracy of the reflection timing results is primarily determined by the geometry of the room, which defines the travelling distance of sounds from the source to the receiver. The accuracy of the amplitude depends on the models of speaker directivity, air absorption coefficients and material properties. It is common that simulation results of the rooms have prominent spikes that are not in the measurement, because surfaces in actual rooms tend to be irregularly shaped and result in more diffuse scattering. This is reflected on the echo density profiles in which echo densities of the measurement results are higher than those of models that only contain specular reflections. Diffuse scattering can smear the timing of reflections, filling gaps between specularly reflected components. The distribution of diffusion depends on different rooms' design. The MMR contains obvious specular reflections and sparse diffusion, while Pallack Hall and Tanna Schulich Hall have a large amount of diffusion, rapidly increasing echo densities in their early reflections. The Wirth Opera Studio has a less evenly distributed diffusion effect. One of the goals of this study was to investigate how specular the sound reflection properties are in concert spaces. Specular reflections are assumed for many room modelling approaches, as well as in the perception of sound directionality in rooms. The results of this study show that these assumptions should be carefully considered, especially for rooms with more irregular reflecting surface profiles.

Chapter 5

Conclusions and Future Work

The presented work builds 3D models for four real rooms in the Schulich School of Music with Matlab and calculates their early reflection responses with given sources and receivers. The results are then compared with the measured impulse responses regarding amplitude, time and echo densities.

Two simulation models, the Image Source Method and the Ray-Tracing Method, are used to generate room impulse responses. Both models are geometric acoustic models, and only specular reflections are considered in the implementation. Up to second order reflections are considered to build the early reflections and the time is limited up 0.1s after the direct sound. The measured rooms include the Music Multimedia Room, Pollack Hall, Tanna Schulich Hall and Wirth Opera Studio. Three different impulse responses with three different microphone positions are recorded in each room. Comparisons between the measurements and simulation results are based on 6 octave bands, in which timing accuracy can be more precisely determined at the higher frequency bands. The four rooms have different reverberant properties according to the differences between measurement results and modeled results. Out of the four, demonstrates the most specular-like reflections with the least diffuse components in the early reflections, while the other two concert halls demonstrate more diffuse scattering within a very short time. The Wirth Opera Studio also has a good diffuse effect in the early part, but the diffusion does not appear to be evenly distributed throughout the room.

Future improvements of the models can be sorted into three main categories:

1. There are various ways the GA algorithm can be improved. The Image Source Method

only works up to second-order reflections and further development should be focused on high order reflection modeling. Regarding the Ray-Tracing Method, methods should be found to improve the efficiency of the algorithm, since it takes hours to generate impulse responses with a large number of rays. Also, neither of the models has good performance at low frequencies, where diffraction effects are more obvious, suggesting that other physical modeling algorithms should be implemented to solve the problem.

2. Models for the real room IR generation can be further refined. More details of the 3D models should be built to improve the accuracy of the simulations. Additionally, more measurements are needed to find the real material properties in each room. Also, the air absorption coefficients and the speaker directivity patterns for each frequency band need to be carefully measured. Other parameters can be obtained from the impulse responses and should be implemented to analyze the results, i.e. Early Decay Time EDT, Clarity C_{te} and the Center Time T_s [57].

3. The last proposed improvements concern the psychoacoustic effects on the impulse responses. Auralization of each virtual room can be implemented according to previous works [58–60] to record the differences between the simulation and measurements. Psychoacoustic experiments based on that can also be made to test the correlations between the modeled and measured impulse responses [61].

Appendix A

Details of Measured Rooms

The pictures below are details of the four measured rooms. Materials of the walls and the positions of the speaker and microphone are annotated.

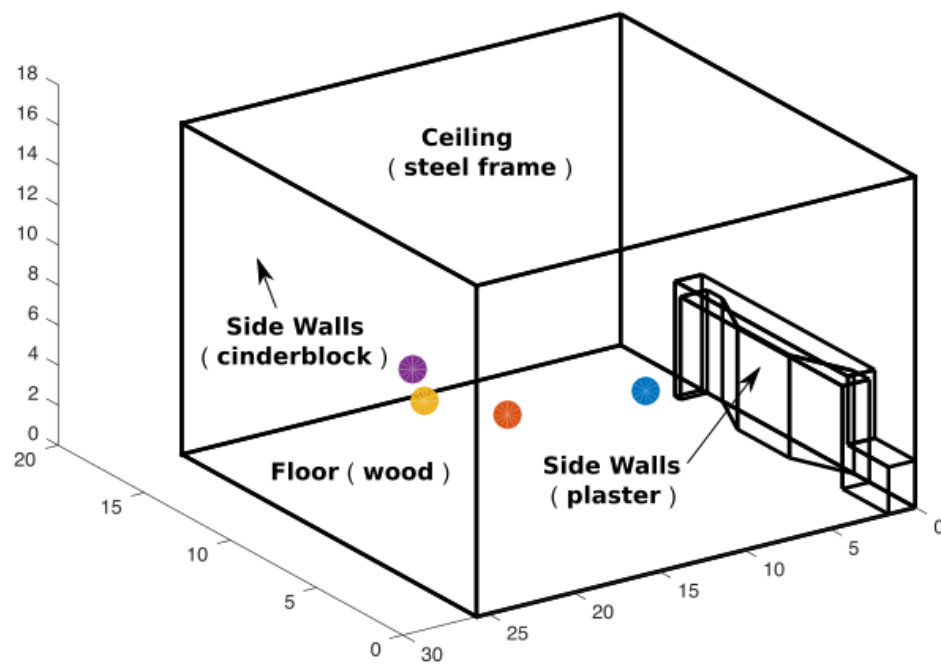


Fig. A.1 Details of the Music Multimedia Room model. The blue point represents the position of the speaker S_1 , the red point represents the first position of the microphone R_1 , the yellow point represents the second position of the microphone R_2 , the purple point denotes the third position of the microphone R_3 . All the points' coordinates are listed in Table 4.4.

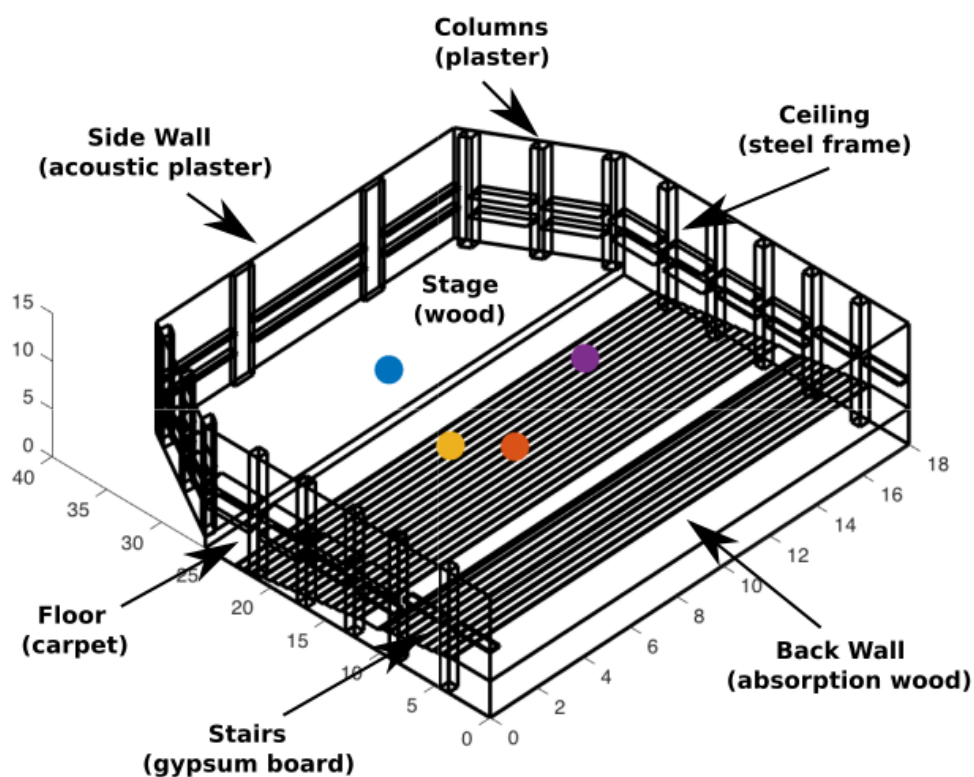


Fig. A.2 Details of the Pollack Hall model. The blue point represents the position of the speaker S_1 , the red point represents the first position of the microphone R_1 , the yellow point represents the second position of the microphone R_2 , the purple point denotes the third position of the microphone R_3 . All the points' coordinates are listed in Table 4.6.

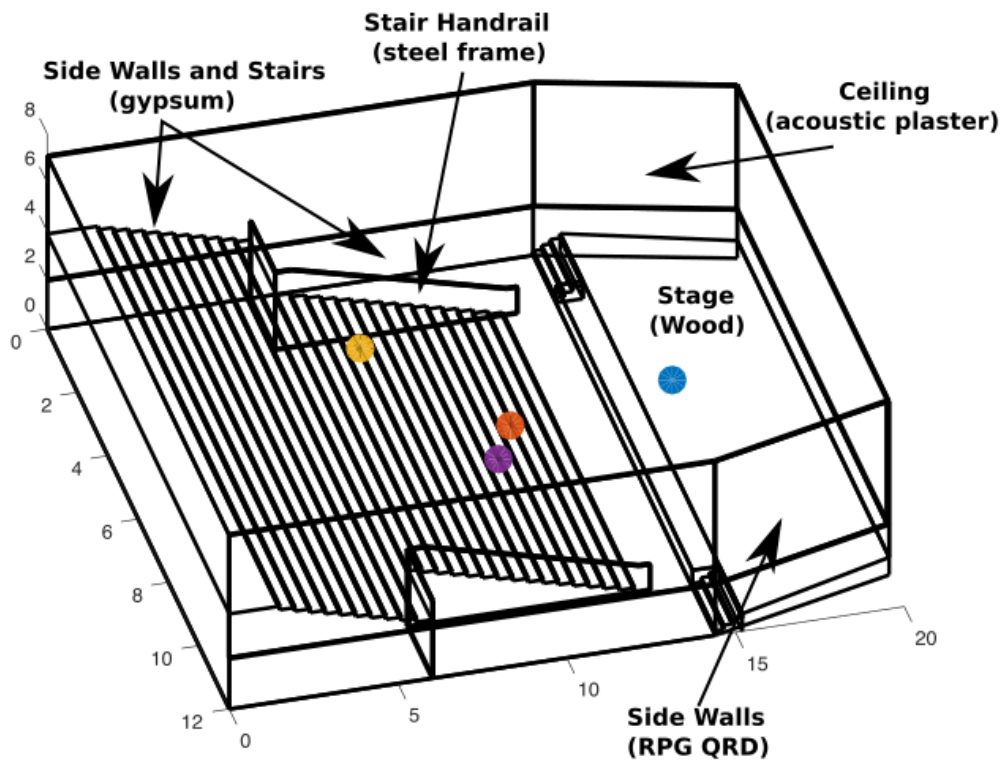


Fig. A.3 Details of the Tanna Schulich Hall model. The blue point represents the position of the speaker S_1 , the red point represents the first position of the microphone R_1 , the yellow point represents the second position of the microphone R_2 , the purple point denotes the third position of the microphone R_3 . All the points' coordinates are listed in Table 4.8.

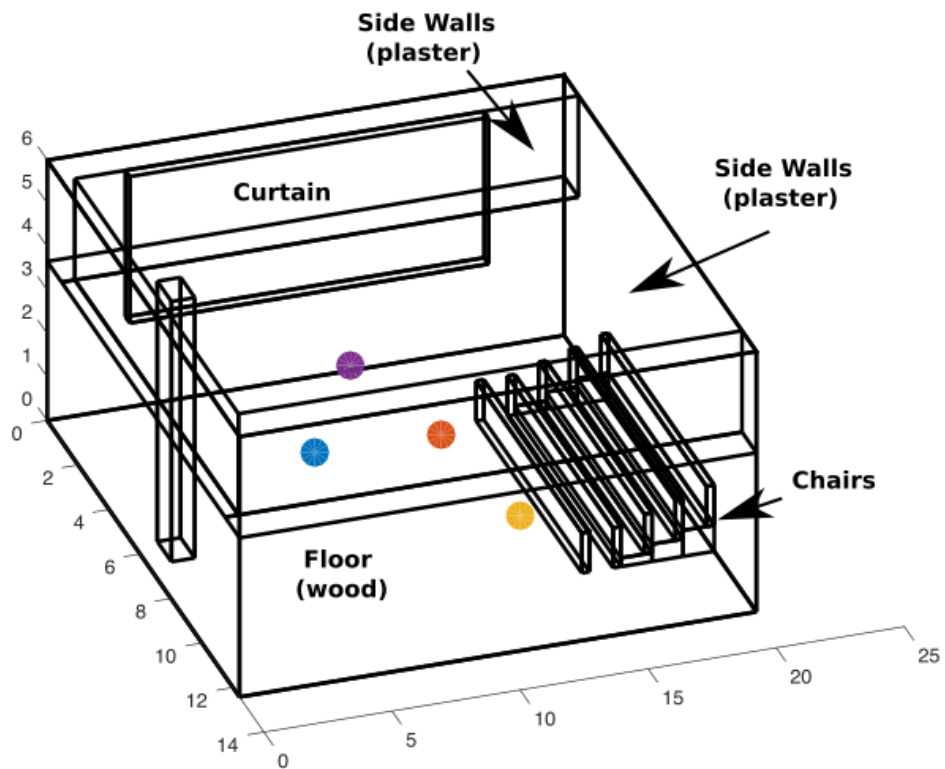


Fig. A.4 Details of the Wirth Opera Studio model. The blue point represents the position of the speaker S_1 , the red point represents the first position of the microphone R_1 , the yellow point represents the second position of the microphone R_2 , the purple point denotes the third position of the microphone R_3 . All the points' coordinates are listed in Table 4.10.

References

- [1] J. S. Abel and P. Huang, “A simple, robust measure of reverberation echo density,” in *Audio Engineering Society Convention 121*, Audio Engineering Society, 2006.
- [2] “Hyperphysics.” <https://hyperphysics.phy-astr.gsu.edu/hbase/Sound/tralon.html>. Accessed: 2016.
- [3] D. O. Elorza, *Room Acoustics Modeling Using the Raytracing Method: Implementation and Evaluation*. 2005.
- [4] H. Kuttruff, *Room acoustics*. Crc Press, 2016.
- [5] J. Borish, “Extension of the image model to arbitrary polyhedra,” *The Journal of the Acoustical Society of America*, vol. 75, no. 6, pp. 1827–1836, 1984.
- [6] L. Savioja and U. P. Svensson, “Overview of geometrical room acoustic modeling techniques,” *The Journal of the Acoustical Society of America*, vol. 138, no. 2, pp. 708–730, 2015.
- [7] M. Vorländer, *Auralization: fundamentals of acoustics, modelling, simulation, algorithms and acoustic virtual reality*. Springer Science & Business Media, 2007.
- [8] H. Lee and B.-H. Lee, “An efficient algorithm for the image model technique,” *Applied Acoustics*, vol. 24, no. 2, pp. 87–115, 1988.
- [9] J. O. Smith, *Physical Audio Signal Processing*. <http://ccrma.stanford.edu/~jos/pasp/>, 2010. online book, 2010 edition.
- [10] W. G. Gardner, “Reverberation algorithms,” in *Applications of digital signal processing to audio and acoustics*, pp. 85–131, Springer, 2002.
- [11] M. Schroeder, B. Atal, and C. Bird, “Digital computers in room acoustics,” *Proc. 4th ICA, Copenhagen M*, vol. 21, 1962.
- [12] A. Krokstad, S. Strom, and S. Sørsdal, “Calculating the acoustical room response by the use of a ray tracing technique,” *Journal of Sound and Vibration*, vol. 8, no. 1, pp. 118–125, 1968.

-
- [13] A. Ondet and J. Barbry, “Modeling of sound propagation in fitted workshops using ray tracing,” *The Journal of the Acoustical Society of America*, vol. 85, no. 2, pp. 787–796, 1989.
- [14] M. R. Hodgson, *Theoretical and physical models as tools for the study of factory sound fields*. PhD thesis, University of Southampton, 1983.
- [15] M. Hodgson, “Measurements of the influence of fittings and roof pitch on the sound field in panel-roof factories,” *Applied Acoustics*, vol. 16, no. 5, pp. 369–391, 1983.
- [16] V. Välimäki, J. Parker, L. Savioja, J. O. Smith, and J. Abel, “More than 50 years of artificial reverberation,” in *Audio Engineering Society Conference: 60th International Conference: DREAMS (Dereverberation and Reverberation of Audio, Music, and Speech)*, Audio Engineering Society, 2016.
- [17] L. Cremer, H. Müller, and T. D. Northwood, “Principles and applications of room acoustics,” 1984.
- [18] D. O. Elorza, *Room acoustics modeling using the raytracing method: implementation and evaluation*. 2005.
- [19] M. Recuero López, “Acústica arquitectónica aplicada,” *Madrid: Paraninfo*, 1999.
- [20] L. Savioja, *Modeling techniques for virtual acoustics*. Helsinki University of Technology Espoo, Finland, 1999.
- [21] C. M. Harris, “Absorption of sound in air versus humidity and temperature,” *The Journal of the Acoustical Society of America*, vol. 40, no. 1, pp. 148–159, 1966.
- [22] Y. W. Lam, “A comparison of three diffuse reflection modeling methods used in room acoustics computer models,” *The Journal of the Acoustical Society of America*, vol. 100, no. 4, pp. 2181–2192, 1996.
- [23] M. Mehta and K. Mulholland, “Effect of non-uniform distribution of absorption on reverberation time,” *Journal of Sound and Vibration*, vol. 46, no. 2, pp. 209–224, 1976.
- [24] C. L. Christensen and J. H. Rindel, “A new scattering method that combines roughness and diffraction effects,” in *Forum Acousticum, Budapest, Hungary*, 2005.
- [25] H. Lehnert and J. Blauert, “Principles of binaural room simulation,” *Applied Acoustics*, vol. 36, no. 3-4, pp. 259–291, 1992.
- [26] V. Hongisto, J. Keränen, and P. Larm, “Simple model for the acoustical design of open-plan offices,” *Acta Acustica united with Acustica*, vol. 90, no. 3, pp. 481–495, 2004.

-
- [27] H. S. Carslaw, *Some Multiform Solutions of the Partial Differential Equations of Physical Mathematics and Their Applications*. Printed at the University Press by Robert MacLehose and Company, 1899.
- [28] L. Cremer, *Die wissenschaftlichen Grundlagen der Raumakustik: Statistische Raumakustik*, vol. 2. S. Hirzel, 1961.
- [29] B. M. Gibbs and D. Jones, “A simple image method for calculating the distribution of sound pressure levels within an enclosure,” *Acta Acustica united with Acustica*, vol. 26, no. 1, pp. 24–32, 1972.
- [30] J. B. Allen and D. A. Berkley, “Image method for efficiently simulating small-room acoustics,” *The Journal of the Acoustical Society of America*, vol. 65, no. 4, pp. 943–950, 1979.
- [31] M. Aretz, P. Dietrich, and M. Vorländer, “Application of the mirror source method for low frequency sound prediction in rectangular rooms,” *Acta Acustica united with Acustica*, vol. 100, no. 2, pp. 306–319, 2014.
- [32] Y. W. Lam, “Issues for computer modelling of room acoustics in non-concert hall settings,” *Acoustical science and technology*, vol. 26, no. 2, pp. 145–155, 2005.
- [33] J. C. Allred and A. Newhouse, “Applications of the monte carlo method to architectural acoustics,” *The Journal of the Acoustical Society of America*, vol. 30, no. 1, pp. 1–3, 1958.
- [34] M. R. Schroeder, “Digital simulation of sound transmission in reverberant spaces,” *The Journal of the Acoustical Society of America*, vol. 47, no. 2A, pp. 424–431, 1970.
- [35] v. M. Vorländer, “Die genauigkeit von berechnungen mit dem raumakustischen schallteilchenmodell und ihre abhängigkeit von der rechenzeit,” *Acta Acustica united with Acustica*, vol. 66, no. 2, pp. 90–96, 1988.
- [36] A. Kulowski, “Error investigation for the ray tracing technique,” *Applied Acoustics*, vol. 15, no. 4, pp. 263–274, 1982.
- [37] M. Vorländer, “Simulation of the transient and steady-state sound propagation in rooms using a new combined ray-tracing/image-source algorithm,” *The Journal of the Acoustical Society of America*, vol. 86, no. 1, pp. 172–178, 1989.
- [38] H. Lehnert, “Systematic errors of the ray-tracing algorithm,” *Applied Acoustics*, vol. 38, no. 2-4, pp. 207–221, 1993.

-
- [39] Z. Xiangyang, C. Ke'an, and S. Jincai, "On the accuracy of the ray-tracing algorithms based on various sound receiver models," *Applied Acoustics*, vol. 64, no. 4, pp. 433–441, 2003.
- [40] G. Naylor, "Treatment of early and late reflections in a hybrid computer model for room acoustics," in *124th ASA Meeting*, 1992.
- [41] G. M. Naylor, "Odeonanother hybrid room acoustical model," *Applied Acoustics*, vol. 38, no. 2-4, pp. 131–143, 1993.
- [42] J. Amanatides, "Ray tracing with cones," in *ACM SIGGRAPH Computer Graphics*, vol. 18, pp. 129–135, ACM, 1984.
- [43] B.-I. Dalenbäck, *A new model for room acoustic prediction and auralization*. Chalmers University of Technology, 1995.
- [44] A. Farina, "Ramsete-a new pyramid tracer for medium and large scale acoustic problems," in *Proc. of Euro-Noise*, vol. 95, 1995.
- [45] M. Barron and A. H. Marshall, "Spatial impression due to early lateral reflections in concert halls: the derivation of a physical measure," *Journal of Sound and Vibration*, vol. 77, no. 2, pp. 211–232, 1981.
- [46] J. S. Suh and P. Nelson, "Measurement of transient response of rooms and comparison with geometrical acoustic models," *The Journal of the Acoustical Society of America*, vol. 105, no. 4, pp. 2304–2317, 1999.
- [47] J. Bradley, H. Sato, and M. Picard, "On the importance of early reflections for speech in rooms," *The Journal of the Acoustical Society of America*, vol. 113, no. 6, pp. 3233–3244, 2003.
- [48] S. Müller and P. Massarani, "Transfer-function measurement with sweeps," *Journal of the Audio Engineering Society*, vol. 49, no. 6, pp. 443–471, 2001.
- [49] G.-B. Stan, J.-J. Embrechts, and D. Archambeau, "Comparison of different impulse response measurement techniques," *Journal of the Audio Engineering Society*, vol. 50, no. 4, pp. 249–262, 2002.
- [50] A. Farina, "Advancements in impulse response measurements by sine sweeps," in *Audio Engineering Society Convention 122*, Audio Engineering Society, 2007.
- [51] I. Bork, "Report on the second international round robin on room acoustical computer simulation," *The Journal of the Acoustical Society of America*, vol. 105, no. 2, pp. 1173–1173, 1999.

-
- [52] I. Bork, “Report on the 3rd round robin on room acoustical computer simulation—part i: Measurements,” *Acta Acustica united with Acustica*, vol. 91, no. 4, pp. 740–752, 2005.
- [53] I. Bork, “Report on the 3rd round robin on room acoustical computer simulation—part ii: Calculations,” *Acta Acustica united with Acustica*, vol. 91, no. 4, pp. 753–763, 2005.
- [54] “The pollack hall.” <https://www.mcgill.ca/music/about-us/facilities/halls/pollack-hall>. Accessed: 2017-6-20.
- [55] “The tanna schulich hall.” <https://www.mcgill.ca/music/about-us/facilities/halls/tanna-schulich-hall>. Accessed: 2017-6-20.
- [56] “The wirth opera studio.” <https://www.mcgill.ca/music/about-us/facilities/research/wirth-opera-studio>. Accessed: 2017-6-20.
- [57] S. Campanini and A. Farina, *A new audicity feature: room objective acoustical parameters calculation module*. na, 2009.
- [58] M. Hodgson, “On the prediction of sound fields in large empty rooms,” *The Journal of the Acoustical Society of America*, vol. 84, no. 1, pp. 253–261, 1988.
- [59] M. Hodgson, “Evidence of diffuse surface reflections in rooms,” *The Journal of the Acoustical Society of America*, vol. 89, no. 2, pp. 765–771, 1991.
- [60] S. Dance, “The representation of fittings in the computer prediction of sound propagation in enclosed spaces,” *Applied Acoustics*, vol. 52, no. 1, pp. 71–83, 1997.
- [61] P. Huang, J. S. Abel, H. Terasawa, and J. Berger, “Reverberation echo density psychoacoustics,” in *Audio Engineering Society Convention 125*, Audio Engineering Society, 2008.